Nonlinear optical response of the α-T_3 model due to the nontrivial topology of the band dispersion

Lei Chen,[1,2] Jack Zuber,[3] Zhongshui Ma,[2,4,*] and Chao Zhang[3,†]
[1]*Department of Applied Physics, Beijing University of Civil Engineering and Architecture, Beijing 102616, China*
[2]*School of Physics, Peking University, Beijing 100871, China*
[3]*School of Physics, University of Wollongong, New South Wales 2522, Australia*
[4]*Collaborative Innovation Center of Quantum Matter, Beijing 100871, China*

(Received 9 May 2019; published 29 July 2019)

We study the electronic contribution to the nonlinear optical response of the α-T_3 model. This model is an interpolation between a graphene ($\alpha = 0$) and dice ($\alpha = 1$) lattice. Using a second-quantized formalism, we calculate the first- and third-order responses for a range of α and chemical potential values as well as considering a band gap in the first-order case. Conductivity quantization is observed for the first-order, while higher-order harmonic generation is observed in the third-order response with the chemical potential determining which applied field frequencies both quantization and harmonic generation occur at. We observe a range of experimentally accessible critical fields between 10^2–10^6 V/m with dynamics depending on α, μ, and the applied field frequency. Our results suggest an α-T_3-like lattice could be an ideal candidate for use in terahertz devices.

DOI: 10.1103/PhysRevB.100.035440

I. INTRODUCTION

Materials with band structures possessing a nontrivial topology have been the subject of growing interest in recent years [1–13] . One of the main characteristics of these materials is that their states are described by an equation analogous to a two-dimensional massless Dirac electron [14,15]. Since this early realization, a lot of work has been done in their ensuing electronic and optical properties [16,17]. These materials have applications in optoelectronics, photonics, and plasmonics and as such have been attracting a significant amount of attention in both theoretical and experimental settings [18–25].

Although various phenomena have been investigated in the framework of the linear response, which is widely used to interpret the low-energy behaviors, the nonlinear response is also important for the elucidation of such electronic structures [26–28]. For example, nonlinear optical properties have been extensively studied for graphene [29–31]. Graphene is thought of as a strong natural nonlinear material, which provides a convenient setting for the study of quantum excitations. Here, optical resonant excitations are allowed at all frequencies up to vacuum ultraviolet [32]. The potentially wide utilizations of graphene in practice follow mainly from its very specific electronic structure. The photoresponse of a graphene sheet has also been the subject of truly intense investigations. The accompanying results convey particularly interesting optical properties such as a strong broadband linear response with a comparatively large optical absorption of visible light and a strong nonlinear response for terahertz (THz) radiation. The linear band structure of graphene has been identified as the origin of the exceptionally strong nonlinear optical response of graphene [33]. Third-order nonlinearities are found to be remarkably strong in single-layer graphene [34–36], with nonlinear susceptibilities several orders of magnitude above those of transparent materials and of the same order as in other resonant materials such as metal nanoparticles. Higher-order harmonic generation (HHG) in single-layer graphene has also been reported recently. The generation of up to the ninth harmonic is demonstrated experimentally using a mid-infrared driving laser [37]. The third harmonic has been observed in few-layer graphene for transitions occurring near the K and M points of the Brillouin zone. It is also found that the nonlinear optical conductivity of graphene would topologically be enhanced in the presence of spin-orbit coupling [38–40]. Inspired by these properties of graphene, there is a growing interest in studying similar structures for potential use in nanoelectronics [41].

One such similar structure is the recently proposed α-T_3 lattice [42]. It is regarded as another simple system featuring massless fermions like graphene. Experimentalists have recently been able to fabricate this trilayer structure of cubic lattices in the (111) direction (for example, SrTiO3/SrIrO3/SrTiO3) [43] or by confining cold atoms to an optical lattice [44]. In the α-T_3 model, the geometry of the honeycomb lattice is augmented by an additional atom that sits at the center of each hexagon coupled to one of the two topologically inequivalent sites of the honeycomb [45–47] (see Fig. 1). A low-energy quasiparticle in the dice lattice is described by the pseudospin-1 Dirac-Weyl equation [44,47]. The spectrum consists of a linear Dirac cone (if it is not gapped) at each Dirac point with an additional dispersionless flat band cutting through the Dirac point. The nontrivial topology emerges due to this flat band [48–53] and results in unusual interaction effects [43,54–59]. The parameter α describes the hopping amplitudes between the additional atom in the honeycomb and the two topologically inequivalent sites. In this way, the α-T_3 model interpolates between the honeycomb lattice of graphene ($\alpha = 0$) and the dice lattice ($\alpha = 1$).

*mazs@pku.edu.cn
†czhang@uow.edu.au

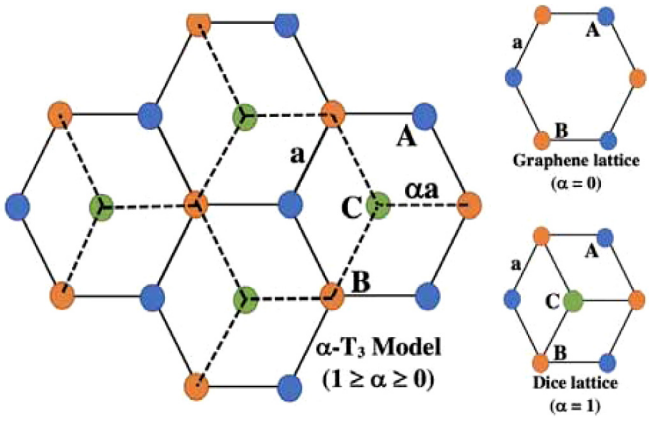

FIG. 1. Graphical representation of the lattice configurations dealt with in the α-T_3 model.

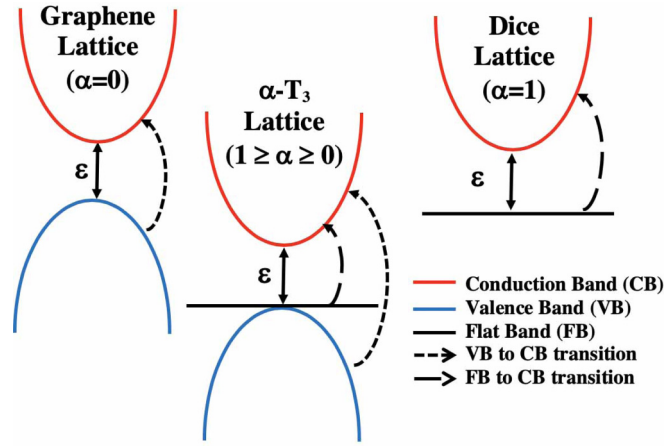

FIG. 2. Schematics of allowed transitions near the Dirac point in graphene, dice lattice, and α-T_3 systems, where ε is the band gap. The dispersion is only for illustration.

The α-T_3 lattice can experience a change from diamagnetic to paramagnetic when the parameter α is tuned from $\alpha = 0$ to 1. Correspondingly, the structures exhibit opposite magnetic behaviors: strongly diamagnetic for undoped graphene, while a large paramagnetic response is seen in the dice (or T_3) lattice. The α-dependent Berry phase [42,60,61] in the α-T_3 model characterizes the unusual topological features and the unconventional quantum Hall effect [62–64]. It has been shown that a two-dimensional (2D) model for $Hg_{1-x}Cd_xTe$ at critical doping can be mapped onto the α-T_3 model with an intermediate parameter $\alpha = 1/\sqrt{3}$ [56]. The α-T_3 model exhibits several unusual electronic properties such as super-Klein tunneling [65–69], minimal conductivity [60], orbital magnetic response [42,70], frequency-dependent magneto-optical conductivity [71,72], and Weiss oscillations [73].

It is well known that graphene displays a universal conductance of $\sigma_0 = e^2/4\hbar$ over a very broad energy range. However, the influence of the flat band introduced in the α-T_3 model on this universal conductance needs further study [74,75]. The flat band in its gapless structure presents a new scenario [76,77] and plays an important role in the transport [78]. Intuitively, the flat band itself has zero conductivity due to its uniformly zero group velocity. However, the interplay between the flat band and the propagating band is predicted to induce a diverging DC conductivity in the presence of disorders [74] or enhance the resulting current in a nonequilibrium situation [78]. It is shown that the particle-hole-symmetric spectrum of massless Dirac fermions in α-T_3 lattice with a flat band provides an opportunity for realizing detectors of radiation in a wide range of photon energies from visible to THz frequencies. One of the characteristic phenomena in the optical response of a dice (or T_3) lattice associated to the flat band is its remarkable affect on nonlinearity.

Figure 2 shows the possible optical transitions in systems without a flat band, with only a flat band and a conduction band, and with conduction, valence, and flat bands. The details of the mechanism underlying this flat-band-dependent nonlinear response remain unaddressed. This may lead to a new aspect of the nonlinear response in comparison with graphene. In particular, an important question that remains to be answered is whether the flat band changes the nonlinear response in a way that is topologically guaranteed [43,44,77], especially in the case of the electron-hole symmetry breaking in the α-T_3 lattice [73,79–81].

For applications in the field of optoelectronics, a comprehensive understanding of nonlinear effects is crucial to the efficient design and analysis of many modern optical devices. For the purposes of application, ribbons made from the α-T_3 lattice have been previously investigated [82–84]. Studies of the optical response of α-T_3 lattice nanoribbons under a weak magnetic field in the terahertz to far-infrared regime found that the interband transitions between the flat band and the propagating bands can enhance the magneto-optical response. The flat band also plays a key role in gap opening and the emergence of a new absorption peak in the optical conductivity [85]. Compelled by such studies, we wish to investigate the effect of the flat band of the α-T_3 lattice on the linear and nonlinear optical properties associated with intersubband transitions of electrons to the conduction band [86,87].

The most consistent description of nonlinear currents, fields, and forces contributing to a nonlinear response requires the use of kinetic theory [88]. We will use a general equation of motion for the tight-binding α-T_3 lattice. By considering the response to an external perturbation, we introduce a density matrix which is the transition- or conditional-probability density for the evolution equation without the perturbation. After expanding it in terms of orthonormal functions, we find terms characterizing the nonlinear responses with matrix products consisting of correlation functions independent of the perturbation. The dynamic response equations are solved in terms of the linear up to the third-order density fluctuations.

The method used here has proved sufficiently general and applicable for any isotropic equilibrium electron distribution function. In the case of linear response, a similar method for the calculation has been well developed [89]. However, our analytical solutions for the third-order and subsequent critical field calculations are unique.

The organization of the paper is as follows: in Sec. II we present the formulation of kinetic theory for the α-T_3 lattice. The nonlinear dynamical response is calculated in Sec. III

along with associated numerical results and discussions. In Sec. IV we present our conclusions.

II. THE α-T_3 MODEL WITH A RADIATION ELECTRIC FIELD

A. Hamiltonian and eigenstates

We adopt the tight-binding description of the α-T_3 model that couples the charge-carrying quasiparticles to the time-dependent radiation field. When a time-dependent external field $\boldsymbol{\mathcal{E}}(t)$ is situated along the x axis, the spatial dependence of the radiation electric field can be neglected in the long-wavelength limit, so that it can be written in the form $\boldsymbol{\mathcal{E}}(t) = \mathcal{E}_x\widehat{e}_x = \mathcal{E}_0 e^{-i\omega t}\widehat{e}_x$. The radiation field is described by a time-dependent vector potential $\mathbf{A}(t) = \mathbf{A}_\omega e^{-i\omega t}$ in the velocity gauge $\boldsymbol{\mathcal{E}}(t) = -(1/c)\partial\mathbf{A}(t)/\partial t$, so that $\mathbf{A}_\omega = -i(c/\omega)\mathcal{E}_x\widehat{e}_x$. Connecting with $\mathbf{A}(t)$, the tight-binding Hamiltonian of the α-T_3 model can be written

$$H(\mathbf{k},\mathbf{A}) = \begin{pmatrix} 0 & \tau_1 f_{\boldsymbol{\Pi}} \cos\varphi & 0 \\ \tau_1 f^*_{\boldsymbol{\Pi}} \cos\varphi & \epsilon & \tau_2 f_{\boldsymbol{\Pi}} \sin\varphi \\ 0 & \tau_2 f^*_{\boldsymbol{\Pi}} \sin\varphi & 0 \end{pmatrix}, \quad (1)$$

where τ_1 and τ_2 are the hopping amplitudes between adjacent triangular lattice, $\boldsymbol{\Pi} = \mathbf{k} + (e/\hbar c)\mathbf{A}$ with $\mathbf{k} = (k_x, k_y)$, and the asterisk denotes the complex conjugation

$$f_{\boldsymbol{\Pi}} = -\left[1 + \sum_\mu \exp(-i\boldsymbol{\Pi}\cdot\mathbf{a}_\mu)\right] \quad (2)$$

is the structure factor formed by linear combinations of Bloch states from the three neighboring sublattices with $\mu = 1$ and 2 for two Bravais lattice vectors $\mathbf{a}_1 = a(\sqrt{3}/2, 3/2)$ and $\mathbf{a}_2 = a(-\sqrt{3}/2, 3/2)$ where a is the intersite distance, ϵ is an onsite energy of the C atom in Fig. 1, and the parameter φ is related to α by $\alpha = \tan\varphi$.

In the absence of the external field $\boldsymbol{\mathcal{E}}(t)$, the three wave functions and associated eigenenergies are found as

$$\xi_0 = \frac{1}{\tau}\begin{pmatrix} -\tau_2 \sin\varphi e^{i2\theta_k} \\ 0 \\ \tau_1 \cos\varphi \end{pmatrix} \quad (3)$$

for $E_0 = 0$ and

$$\xi_{\mathbf{k},\lambda} = \frac{1}{\sqrt{E_\lambda^2 + |f_{\mathbf{k}}|^2\tau^2}}\begin{pmatrix} \tau_1 f_{\boldsymbol{\Pi}} \cos\varphi \\ E_\lambda \\ \tau_2 f^*_{\boldsymbol{\Pi}} \sin\varphi \end{pmatrix} \quad (4)$$

for $E_\lambda = (\epsilon + \lambda\sqrt{\epsilon^2 + 4|f_{\boldsymbol{\Pi}}|^2\tau^2})/2$, respectively, where $\lambda = \pm 1$ corresponds to the conduction (+) and valence (−) bands and $\tau^2 = \tau_1^2\cos^2\varphi + \tau_2^2\sin^2\varphi$. The states $\xi_{\mathbf{k},s}$ $(s = 0, \pm 1)$ satisfy the orthogonality condition $\langle\xi_{\mathbf{k},s}|\xi_{\mathbf{k}',s'}\rangle = \delta_{ss'}\delta(\mathbf{k} - \mathbf{k}')$.

The structure factor $f_{\boldsymbol{\Pi}}$ can be expanded in powers of $\mathbf{A}(t)$ as follows:

$$f_{\boldsymbol{\Pi}} = f_{\mathbf{k}} - \sum_{n=1}\frac{1}{n!}\left(-i\frac{e}{\hbar c}\right)^n \mathcal{A}^{(n)}(\mathbf{k}), \quad (5)$$

where $\mathcal{A}^{(n)}(\mathbf{k}) = \sum_\mu e^{-i(\mathbf{k}\cdot\mathbf{a}_\mu + n\omega t)}(\mathbf{A}_\omega\cdot\mathbf{a}_\mu)^n$ and $f_{\mathbf{k}}$ is the structure factor in the absence of an external field.

Equation (5) is a result of a direct expansion of the Hamiltonian in terms of the applied field. An equivalent quantum formalism based on Floquet states can also be used to treat the problem of electron coupled to a boson field. The formalism was used previously in electron-photon coupling in graphene [90,91], electron transport in two-dimensional semiconductors [92], and article diffusion with electron-phonon scattering [93]. In the present system, the Floquet state includes electron-photon coupling to all orders and is an exact eigenstate of the Hamiltonian (1). Using Floquet states or a Magnus expansion one can construct the full density matrix which includes all orders of electron-photon coupling [94–98]. Conversely, our formalism expands first the Hamiltonian in successive orders of electron-photon coupling and only requires calculation of the density matrix and associated current response for each order that will be considered. As such, our results are equivalent to the other approaches at each order of electron-photon coupling. The system under a more complicated nonresonant field has been recently investigated using a Magnus expansion within the Floquet formalism [80].

Using Eq. (5), the time-dependent Hamiltonian can be written in the form

$$H(\mathbf{k},t) = H_0(\mathbf{k}) + H_{em}(\mathbf{k},t), \quad (6)$$

where $H_0(\mathbf{k})$ is independent of $\mathbf{A}(t)$ with the eigenstates ξ_0 and $\xi_{\mathbf{k},\lambda}$, while $H_{em}(\mathbf{k},t)$ contains the interaction of electrons with the external field and is given by

$$H_{em}(\mathbf{k},t) = -\sum_{n=1}\frac{1}{n!}\left(-i\frac{e}{\hbar c}\right)^n \begin{pmatrix} 0 & \tau_1\mathcal{A}^{(n)}\cos\varphi & 0 \\ \tau_1(-1)^n\mathcal{A}^{(n)*}\cos\varphi & 0 & \tau_2\mathcal{A}^{(n)}\sin\varphi \\ 0 & \tau_2(-1)^n\mathcal{A}^{(n)*}\sin\varphi & 0 \end{pmatrix}. \quad (7)$$

We use the eigenstates of $H_0(\mathbf{k})$ to write the time-dependent Hamiltonian $H(\mathbf{k},t)$ in the second quantization form. This is done via the standard procedure of writing the time-dependent wave function as $\psi(t) = \sum_{\mathbf{k}} a_{\mathbf{k},0}(t)\xi_0 + \sum_{\mathbf{k},\lambda} a_{\mathbf{k},\lambda}(t)\xi_{\mathbf{k},\lambda}$, where the creation and annihilation operators of Bloch states $a^\dagger_{\mathbf{k},s}$ and $a_{\mathbf{k},s}$ satisfy the anticommutation relations $\{a^\dagger_{\mathbf{k},s}, a^\dagger_{\mathbf{k}',s'}\} = \{a_{\mathbf{k},s}, a_{\mathbf{k}',s'}\} = 0$ and $\{a_{\mathbf{k},s}, a^\dagger_{\mathbf{k}',s'}\} = \delta_{ss'}\delta(\mathbf{k} - \mathbf{k}')$ where $s = 0, \pm 1$. In terms of $a^\dagger_{\mathbf{k},s}$ and $a_{\mathbf{k},s}$, the Hamiltonian in Eq. (7) is written

$$\begin{aligned} H = &\sum_{k,\lambda}[E_\lambda a^\dagger_{\mathbf{k},\lambda}a_{\mathbf{k},\lambda} + (M_{\lambda,0}(\mathbf{k})a^\dagger_{\mathbf{k},\lambda}a_{\mathbf{k},0} + \text{H.c.}) \\ &+ M_{\lambda,\lambda}(\mathbf{k})a^\dagger_{\mathbf{k},\lambda}a_{\mathbf{k},\lambda} + M_{\lambda,-\lambda}(\mathbf{k})a^\dagger_{\mathbf{k},\lambda}a_{\mathbf{k},-\lambda}], \end{aligned} \quad (8)$$

where $M_{i,j}=\sum_n A_x^n M_{i,j}^{(n)}$ with $i,j=0,\lambda$ and $M_{i,j}^{(n)}(\mathbf{k})=[M_{j,i}^{(n)}(\mathbf{k})]^*$ are the matrix units. For simplicity, we set $\tau_1=\tau_2=\tau$ in our calculations. The $M_{i,j}$ can be found explicitly:

$$M_{\lambda,0}^{(2n-1)}(\mathbf{k})=\frac{2\tau B^{2n-1}}{(2n-1)!}\frac{E_\lambda \sin 2\varphi e^{i\theta_k}}{\widetilde{E}_\lambda(\mathbf{k})}\sin\frac{\sqrt{3}}{2}k_x a\,\sin\frac{3}{2}K_y a,$$

$$M_{\lambda,0}^{(2n)}(\mathbf{k})=i\frac{2\tau B^{2n}}{(2n)!}\frac{E_\lambda \sin 2\varphi e^{i\theta_k}}{\widetilde{E}_\lambda(\mathbf{k})}\cos\frac{\sqrt{3}}{2}k_x a\,\sin\frac{3}{2}K_y a,$$

$$M_{\lambda,\lambda}^{(2n-1)}(\mathbf{k})=i\frac{2\tau B^{2n-1}}{(2n-1)!}\frac{2E_\lambda\tau|f_\mathbf{k}|}{\widetilde{E}_\lambda^2(\mathbf{k})}\sin\frac{\sqrt{3}}{2}k_x a\,\cos\frac{3}{2}K_y a,$$

$$M_{\lambda,\lambda}^{(2n)}(\mathbf{k})=-\frac{2\tau B^{2n}}{(2n)!}\frac{2E_\lambda\tau|f_\mathbf{k}|}{\widetilde{E}_\lambda^2(\mathbf{k})}\cos\frac{\sqrt{3}}{2}k_x a\,\cos\frac{3}{2}K_y a,$$

$$M_{\lambda,-\lambda}^{(2n-1)}(\mathbf{k})=i\frac{2\tau B^{2n-1}}{(2n-1)!}\frac{\tau|f_\mathbf{k}|\sin\frac{\sqrt{3}}{2}k_x a\left[\epsilon\,\cos\frac{3}{2}K_y a+i(2E_\lambda-\epsilon)\cos 2\varphi\,\sin\frac{3}{2}K_y a\right]}{\widetilde{E}_\lambda(\mathbf{k})\widetilde{E}_{-\lambda}(\mathbf{k})},$$

and

$$M_{\lambda,-\lambda}^{(2n)}(\mathbf{k})=-\frac{2\tau B^{2n}}{(2n)!}\frac{\tau|f_\mathbf{k}|\cos\frac{\sqrt{3}}{2}k_x a\left[\epsilon\cos\frac{3}{2}K_y a+i(2E_\lambda-\epsilon)\cos 2\varphi\,\sin\frac{3}{2}K_y a\right]}{\widetilde{E}_\lambda(\mathbf{k})\widetilde{E}_{-\lambda}(\mathbf{k})},$$

where $\widetilde{E}_\lambda(\mathbf{k})=\sqrt{E_\lambda^2+\tau^2|f_\mathbf{k}|^2}$, $B=-i\sqrt{3}ea/(2\hbar c)$, and $K_y=k_y+2/(3a)\theta_k$ with the argument of $f_\mathbf{k}$:

$$\theta_k=-\tan^{-1}\frac{2\cos\frac{\sqrt{3}}{2}k_x a\,\sin\frac{3}{2}k_y a}{1+2\cos\frac{\sqrt{3}}{2}k_x a\,\cos\frac{3}{2}k_y a}. \tag{9}$$

In our analysis, we shall calculate the current response up to the third order. Certain conditions must be met in order for the third-order term to represent the leading-order nonlinear effect. Here, the parameter defining the nonlinear effect is $\mathcal{K}=(e/hc)\mathbf{A}\cdot\mathbf{a}$. Since $\mathbf{A}=-c/i\omega\boldsymbol{\mathcal{E}}$, $\mathcal{K}$ is the ratio of the work done by the electric field over the distance of the lattice constant to the photon energy. Our results cover typical applied fields of 10^2 to 10^5 V/m. For the lattice constant $a=0.142$ nm, $e\mathcal{E}a$ is or the order of 1.42×10^{-5} to 1.42×10^{-2} meV. To only consider a few leading terms of Eq. (5) and truncate the series after $\mathcal{A}^{(3)}$, $\mathcal{K}$ should be smaller than 1. This requires the photon energy $\hbar\omega_c>e\mathcal{E}a$ which corresponds to $\omega_c>0.00355$ THz. Therefore, although all our plots start from zero frequency, our results should be valid for any frequency higher than ω_c. As we shall show, this region contains all properties of interest.

B. Reduced density matrix and its equation of motion

We define the reduced density matrix $\rho_{s,s'}(\mathbf{k},t)=\langle a_{\mathbf{k},s}^\dagger(t)a_{\mathbf{k},s'}(t)\rangle$. This is a matrix in band space whose value is the average momentum-conserving interband ($s\neq s'$) and intraband ($s=s'$) transitions.

Using the following equation of motion for the Bloch states,

$$i\hbar\frac{\partial a_{\mathbf{k},s}}{\partial t}=\sum_\lambda M_{\lambda,0}\delta_{s,\lambda}a_{\mathbf{k},0}+\sum_\lambda(E_\lambda\delta_{s,\lambda}+M_{0,\lambda}\delta_{s,0}+M_{\lambda,\lambda}\delta_{s,\lambda}+M_{-\lambda,\lambda}\delta_{s,-\lambda})a_{\mathbf{k},\lambda}, \tag{10}$$

the reduced density matrix can be deduced by computing its own equation of motion $i\hbar[d\rho_{s,s'}(\mathbf{k})/dt]=\langle[a_{\mathbf{k},s}^\dagger a_{\mathbf{k},s'},H(t)]\rangle$. We obtain the following set of coupled three-level equations:

$$\left(i\hbar\frac{\partial}{\partial t}+E_s-E_{s'}+M_{s,s}-M_{s',s'}\right)\rho_{s,s'}=-M_{0,s}\rho_{0,s'}+M_{s',0}\rho_{s,0}-M_{-s,s}\rho_{-s,s'}+M_{s',-s'}\rho_{s,-s'}-\sum_\lambda(\delta_{s,0}M_{\lambda,0}\rho_{\lambda,s'}-\delta_{s',0}M_{0,\lambda}\rho_{s,\lambda}). \tag{11}$$

To isolate different order optical response terms, we expand $\rho_{s,s'}$ in powers of $\mathbf{A}$ such that $\rho_{s,s'}=\sum_m A_x^m\rho_{s,s'}^{(m)}$. The temporal derivative of $\rho_{s,s'}^{(m)}$ can then be expressed as

$$\begin{aligned}\left(i\hbar\frac{\partial}{\partial t}+E_s-E_{s'}\right)\rho_{s,s'}^{(m)}&=-\sum_n\left(M_{s,s}^{(n)}-M_{s',s'}^{(n)}\right)\rho_{s,s'}^{(m-n)}\\&\quad-\sum_n\left(M_{0,s}^{(n)}\rho_{0,s'}^{(m-n)}-M_{s',0}^{(n)}\rho_{s,0}^{(m-n)}\right)\\&\quad-\sum_n\left(M_{-s,s}^{(n)}\rho_{-s,s'}^{(m-n)}-M_{s',-s'}^{(n)}\rho_{s,-s'}^{(m-n)}\right)\\&\quad-\sum_{n,\lambda=\pm1}\left(\delta_{s,0}M_{\lambda,0}^{(n)}\rho_{\lambda,s'}^{(m-n)}-\delta_{s',0}M_{0,\lambda}^{(n)}\rho_{s,\lambda}^{(m-n)}\right).\end{aligned} \tag{12}$$

The Fourier-transformed components $\rho^{(m)}_{s,s'}(\mathbf{k},\omega)$ can be obtained from this recursion relation given the zeroth-order reduced density matrix terms are defined by $\rho^{(0)}_{s,s'}(k) = \delta_{s,s'} n_s(k)$, where $n_s(k) = [1 + e^{[E_s(k)-\mu]/k_BT}]^{-1}$ is the Fermi-Dirac distribution at temperature T and chemical potential μ.

The first-order density matrices are $\rho^{(1)}_{0,0}(\mathbf{k},\omega) = \rho^{(1)}_{\lambda,\lambda}(\mathbf{k},\omega) = 0$,

$$\rho^{(1)}_{\lambda,0}(\mathbf{k},\omega) = -M^{(1)}_{0,\lambda}\frac{n_0 - n_\lambda}{\hbar\omega + E_\lambda}, \tag{13}$$

<?vsp 2pt ?>$\rho^{(1)}_{0,\lambda}(\mathbf{k},\omega) = \rho^{(1)*}_{\lambda,0}(\mathbf{k},-\omega)$, and

$$\rho^{(1)}_{\lambda,-\lambda}(\mathbf{k},\omega) = M^{(1)}_{-\lambda,\lambda}\frac{n_\lambda - n_{-\lambda}}{\hbar\omega + (E_\lambda - E_{-\lambda})}. \tag{14}$$

The second, third, and higher orders can be found in the same way. The analytical expressions of $\rho^{(2)}_{s,s'}(\mathbf{k},\omega)$ and $\rho^{(3)}_{s,s'}(\mathbf{k},\omega)$ are given in Appendix A.

III. NONLINEAR DYNAMICAL RESPONSE

The current response is calculated using the standard electrodynamics formula

$$\begin{aligned}\langle\mathbf{J}\rangle_\omega &= c\langle\nabla_{\mathbf{A}}H(\mathbf{k},t)\rangle \\ &= c\sum_{k,\lambda,n,m} n\mathbf{A}^{n+m-1}_\omega\big[\mathbf{M}^{(n)}_{\lambda,0}(\mathbf{k})\rho^{(m)}_{\lambda,0} + \mathbf{M}^{(n)}_{0,\lambda}(\mathbf{k})\rho^{(m)}_{0,\lambda} \\ &\quad + \mathbf{M}^{(n)}_{\lambda,\lambda}(\mathbf{k})\rho^{(m)}_{\lambda,\lambda} + \mathbf{M}^{(n)}_{\lambda,-\lambda}(\mathbf{k})\rho^{(m)}_{\lambda,-\lambda}\big],\end{aligned} \tag{15}$$

where the conditions $n \geqslant 1 \in \mathbb{Z}$ and $m \geqslant 0 \in \mathbb{Z}$ are used to determine the different order optical responses. For example, $(n,m) = \{(1,1),(2,0)\}$ for the first order, $(n,m) = \{(2,1),(3,0),(1,2)\}$ for the second order, and so on.

The full nonlinear current is then $\langle\mathbf{J}\rangle_\omega = \sigma^{(1)}_x\mathcal{E}_x + \sigma^{(2)}_x\mathcal{E}_x\mathcal{E}_x + \sigma^{(3)}_x\mathcal{E}_x\mathcal{E}_x\mathcal{E}_x + \cdots$, where $\sigma^{(i)}_x$ $(i = 1,2,3,\ldots)$ are the nonzero components of the ith-order conductivity tensor. To yield proper dimensions, the ith-order conductivity must be dependent on the applied field for $i \geqslant 2$ and is given by $\sigma^{(i)} = \sigma^{(i)}_x\mathcal{E}^{i-1}_x$.

A. Linear optical conductivity: Single-photon processes

The nonzero component of the first-order optical conductivity tensor is found as

$$\begin{aligned}\frac{\mathrm{Re}\left(\sigma^{(1)}_x\right)}{\sigma^{(1)}_0} &= 2\pi(\sqrt{3}a\tau)^2\Bigg\{\sin^2(2\varphi)\sum_{k,\lambda}\frac{E^2_\lambda\Lambda(\mathbf{k})(n_0 - n_\lambda)}{\widetilde{E}^2_\lambda(\mathbf{k})}\frac{\delta(\hbar\omega + E_\lambda) + \delta(\hbar\omega - E_\lambda)}{E_\lambda} \\ &\quad - \sum_{k,\lambda}\frac{\tau^2|f_\mathbf{k}|^2(n_\lambda - n_{-\lambda})[\epsilon^2\Lambda'(\mathbf{k}) + (\epsilon^2 + 4\tau^2|f_\mathbf{k}|^2)\cos^2(2\varphi)\Lambda(\mathbf{k})]}{\widetilde{E}^2_\lambda(\mathbf{k})\widetilde{E}^2_{-\lambda}(\mathbf{k})}\frac{\delta(\hbar\omega + E_\lambda - E_{-\lambda})}{E_\lambda - E_{-\lambda}} \\ &\quad + \sum_{k,\lambda}\Bigg[\frac{2E^2_\lambda\Lambda(\mathbf{k})n_\lambda}{\widetilde{E}^2_\lambda(\mathbf{k})}\left(1 - \frac{E_{-\lambda}}{E_\lambda}\right)\sin^2(2\varphi) \\ &\quad - \frac{\tau^2|f_\mathbf{k}|^2(n_\lambda - n_{-\lambda})\epsilon^2\Lambda'(\mathbf{k}) + (\epsilon^2 + 4\tau^2|f_\mathbf{k}|^2)\cos^2(2\varphi)\Lambda(\mathbf{k})}{\widetilde{E}^2_\lambda(\mathbf{k})\widetilde{E}^2_{-\lambda}(\mathbf{k})}\Bigg]\frac{\delta(\hbar\omega)}{E_\lambda - E_{-\lambda}}\Bigg\},\end{aligned} \tag{16}$$

where the universal conductivity $\sigma^{(1)}_0 = e^2/(2\hbar)$,

$$\Lambda(\mathbf{k}) = \sin^2\left(\frac{\sqrt{3}}{2}k_x a\right)\sin^2\left(\frac{3}{2}K_y a\right), \tag{17}$$

and

$$\Lambda'(\mathbf{k}) = \sin^2\left(\frac{\sqrt{3}}{2}k_x a\right)\cos^2\left(\frac{3}{2}K_y a\right). \tag{18}$$

The two $\delta(\hbar\omega)$ terms in Eq. (16) are *intraband* (Drude) conductivity terms, while the other terms are due to the *interband* conductivity. We observe that the flat band (n_0) does not contribute to the intraband conductivity. Physically, this is due to its uniformly zero group velocity. The Dirac peak around $\omega = 0$ can be broadened into a Drude peak by considering residual scattering whereby

$$\delta(\hbar\omega) = \frac{1}{\pi}\frac{\gamma}{(\hbar\omega)^2 + \gamma^2}, \tag{19}$$

where γ is the scattering rate, typically of the order $10^{-3}\mu$. For terahertz frequencies, unless μ is exceptionally large, the intraband conductivity will not be appreciable.

The third term contains only flat-to-conduction band transitions and is the only interband term remaining for the extremal value of $\alpha = 1$ (dice lattice). Finally, we observe that the $\delta(\hbar\omega + E_\lambda - E_{-\lambda})$ term contains only valence-to-conduction band transitions and is the only interband term for graphene ($\alpha = 0$). This agrees with other dynamical conductivity models for graphene where the flat band is not present and the movable atom is decoupled from the hexagonal lattice.

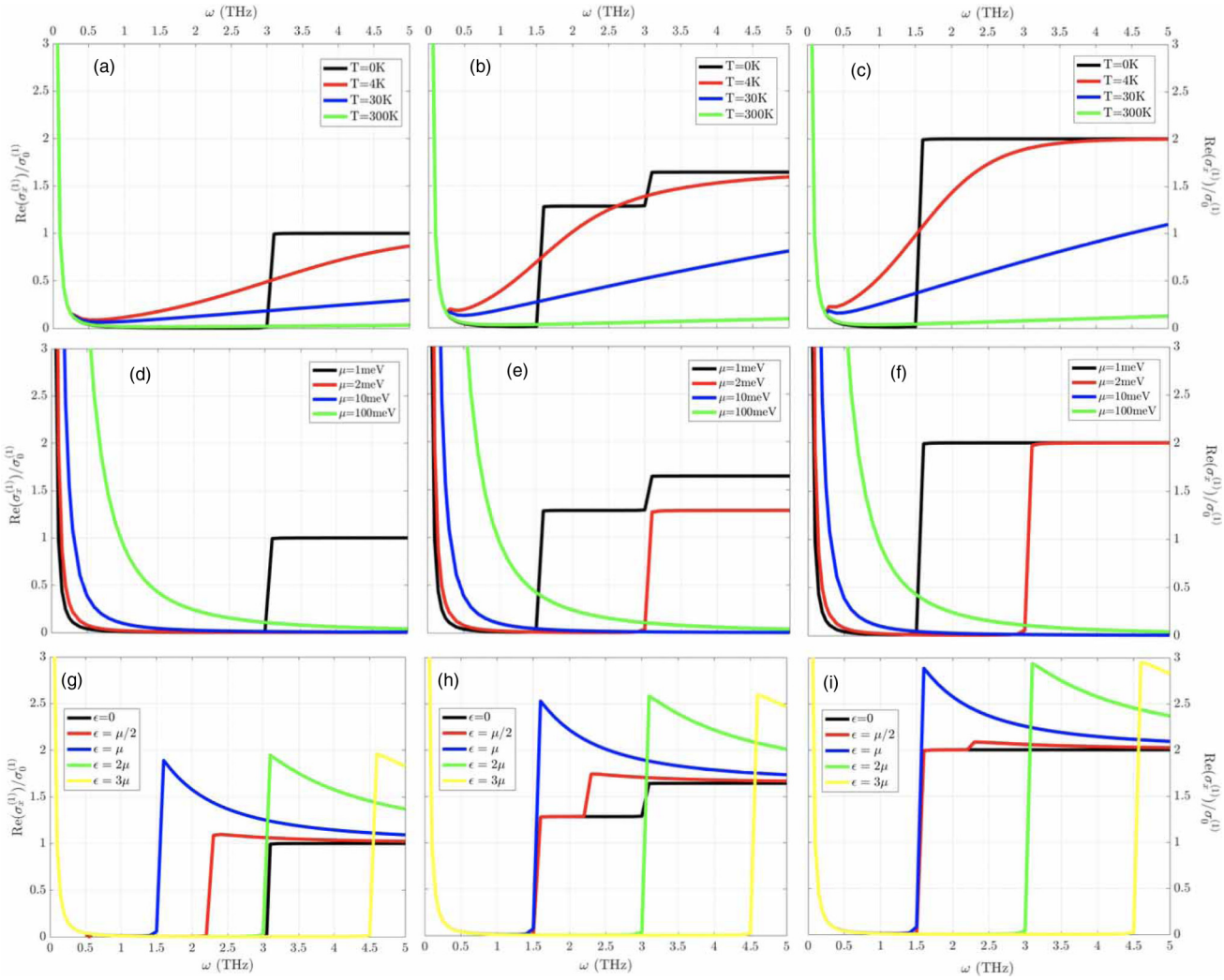

FIG. 3. First-order interband conductivities using $a = 0.142$ nm, $\tau_1 = \tau_2 = 3$ eV, and the following parameter ensembles: (a) $\alpha = 0$, $\mu = 1$ meV, $\epsilon = 0$. (b) $\alpha = 0.5$, $\mu = 1$ meV, $\epsilon = 0$. (c) $\alpha = 1$, $\mu = 1$ meV, $\epsilon = 0$. (d) $\alpha = 0$, $T = 0$ K, $\epsilon = 0$. (e) $\alpha = 0.5$, $T = 0$ K, $\epsilon = 0$. (f) $\alpha = 1$, $T = 0$ K, $\epsilon = 0$. (g) $\alpha = 0$, $T = 0$ K, $\mu = 1$ meV. (h) $\alpha = 0.5$, $T = 0$ K, $\mu = 1$ meV. (i) $\alpha = 1$, $T = 0$ K, $\mu = 1$ meV.

To numerically evaluate Eq. (16) we let $\sum_k \to \frac{1}{(2\pi)^2}\iint_{\mathrm{BZ}} dk_x dk_y$ where the Brillouin zone (BZ) is the 2D region

$$\mathrm{BZ} = \Big\{(k_x, k_y) \in \mathbb{R}^2 : |k_y| \leqslant \frac{2\pi}{3a} \cap |k_y + \sqrt{3}k_x| \leqslant \frac{4\pi}{3a} \cap |k_y - \sqrt{3}k_x| \leqslant \frac{4\pi}{3a}\Big\}. \quad (20)$$

The first-order conductivity results for a number of different band-gap, temperature, chemical potential, and α values in Fig. 3.

We observe first that there is a stable quantization of the first-order conductivity for any value of α so long as $\epsilon = T = 0$. For $\alpha = 0$ the conductivity is quantized at a value of σ_0 and stable for $\hbar\omega/\mu > 2$, for $\alpha = 1$ the conductivity is quantized at a value of $2\sigma_0$ and stable for $\hbar\omega/\mu > 1$. For $0 < \alpha < 1$ we observe a superposition between these two quantization regimes. This phenomenon has been predicted by previous models [47,63]. The uniqueness of our first-order calculations is in how a nonzero band gap (ϵ) or temperature (T) affects the stability of these quantized conductivity values.

From Figs. 3(g)–3(i), a nonzero ϵ has no effect on the stability of flat band to Dirac cone transitions. This is evidenced by the $\alpha = 1$ plots staying flat for $\epsilon \neq 0$. Also, the frequency at which quantization jumps occurs is unchanged if $\epsilon \leqslant \mu$ but increased if $\epsilon > \mu$. The stability of flat band to conduction band transitions is because the flat band gains velocity with $\epsilon \neq 0$ and moves up in momentum space with the conduction band. The latter phenomenon is due to an increased band gap pushing the upper Dirac cone above the Fermi level leading to an increased photon energy needed to excite charge carriers from the flat band to the conduction band.

The stability of valence-to-conduction band transitions ($\alpha = 0$) is broken by a nonzero band gap regardless of its magnitude. This is because considering a band gap imposes an inversion-breaking perturbation mathematically shown by the Λ' term. Furthermore, the frequency at which the conductivity jump occurs is decreased for $\epsilon < \mu$ and increased for $\epsilon > \mu$.

The $\alpha = 0.5$ case is once again a superposition of the two extremal value conductivities as expected.

To investigate nonzero temperatures, we consider that when setting $\epsilon = 0$, the first-order conductivity formula simplifies significantly to

$$\frac{\mathrm{Re}\left(\sigma_x^{(1)}\right)}{\sigma_0^{(1)}} = 2\pi(\sqrt{3}a\tau)^2\Bigg\{\sum_k \frac{\Lambda(\mathbf{k})}{E_+}\delta(\hbar\omega)(n_+ - n_-) + \sin^2(2\varphi)\sum_{k,\lambda}\frac{\Lambda(\mathbf{k})}{E_\lambda}\delta(\hbar\omega + \lambda|f_\mathbf{k}|)(n_+ - n_-) + \frac{\cos^2(2\varphi)}{2}\sum_{k,\lambda}\frac{\Lambda(\mathbf{k})}{E_\lambda}\delta(\hbar\omega + 2\lambda|f_\mathbf{k}|)(n_+ - n_-)\Bigg\}. \tag{21}$$

The expression in Eq. (21) reveals important topological information about the system. Using the Chern-Kubo formula one can identify

$$\left(\frac{\phi_B}{\pi}\right)^2 = \cos^2(2\varphi) \text{ and } 1 - \left(\frac{\phi_B}{\pi}\right)^2 = \sin^2(2\varphi), \tag{22}$$

where ϕ_B is the Berry phase [47,63]. Thus, the first-order optical conductivity reveals information about the geometry/topology of the lattice without the need for a magnetic field.

The plots in Figs. 3(a)–3(c) show that the first-order conductivity quantization occurs only for very low temperatures $T < 4$ K. The nonzero temperature curves clearly approach their $T = 0$ K values for each value of α as $T \to 0$.

Figures 3(d)–3(f) show that by varying the chemical potential of the material one can engineer the desired frequencies at which the conductivity jumps occur. In practice this could be done by doping the sample and would allow users to select conductivity modes based only upon electric field frequencies without need for a magnetic field like in quantum Hall setups.

Now, if we look at very high frequencies, which correspond to maximal dispersion energies, we see the breakdown of the conductivity quantization.

We see that for frequencies $\omega \geqslant 10^{15}$ Hz the quantization breaks down as the photon energies approach the energy of the top of the conduction band. The peaks occur at the delta-function maxima for terms 2 and 3 in Eq. (21) as expected. The second peak is much smaller as the photon energy is above the conduction band maximum and is hence somewhat masked in the top plot of Fig. 4.

To showcase the validity of this model in the terahertz range, if one approximates the dispersion as a linear function in $\mathbf{k}$ such that $E_\lambda \approx \frac{3a\tau}{2}|\mathbf{k}|$ and sets $T = 0$, the first-order conductivity further reduces to

$$\frac{\mathrm{Re}\left(\sigma_x^{(1)}\right)}{\sigma_0^{(1)}} = \cos^2(2\varphi)[4\mu\delta(\hbar\omega) + \theta(\hbar\omega - 2\mu)] + \sin^2(2\varphi)\{2[2\mu\delta(\hbar\omega) + \theta(\hbar\omega - \mu)]\}. \tag{23}$$

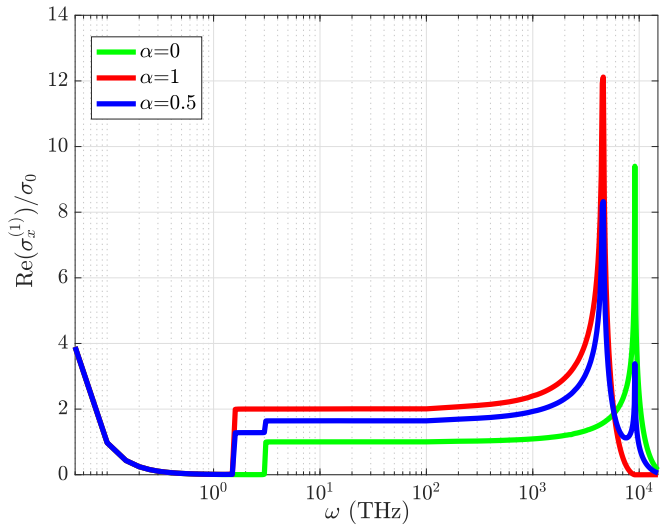

FIG. 4. First-order conductivity at high frequencies for $\epsilon = 0$, $T = 0$ K, and $\mu = 1$ meV at high frequencies.

This expression is identical to the Kubo formula for this problem [63] and agrees perfectly with our results in the low-frequency range in Figs. 3(d)–3(f). Hence, we conclude that for experimentally viable frequencies ($\omega < 10^{15}$ Hz) a linear approximation is appropriate. However, a linear approximation to the dispersion is not topologically appropriate for $\epsilon \neq 0$.

B. Nonlinear optical conductivity: Two photon processes

Due to the k symmetry of second-order reduced density matrix terms, we find that the second-order optical conductivity $\mathrm{Re}\,(\sigma_x^{(2)}) = 0$. By directly summing over all terms proportional to A^2 in Eq. (15), one can show that the second-order current vanishes. An example of how this calculation is carried out is shown in Appendix A. This result is both consistent with accepted results for graphene and the symmetry $\mathbf{J}(\mathbf{A}) = -\mathbf{J}(-\mathbf{A})$.

Since $\epsilon \neq 0$ changes quantization phenomena (which does not occur in the third order) and the frequencies at which the conductivity harmonics occur (which can equivalently be done by changing μ) we consider $\epsilon = 0$ from the outset in this section.

Furthermore, from the results for the first-order conductivity we observe a linear approximation in $\mathbf{k}$ provides a very accurate description of the system in the terahertz regime. So, we relegate the full nonlinear dispersion results to Appendix B and provide the results for a linear dispersion in this section. First, the third-order intraband tensor component is given by

$$\frac{\mathrm{Re}\left(\sigma_x^{(3),\mathrm{intra}}\right)}{\sigma_0^{(3)}} = \frac{27\pi\tau^4}{256\mu}\delta^3(\hbar\omega)\left(\sin^4(2\varphi) + \frac{\cos^2(2\varphi)\sin^2(2\varphi)}{2} + \frac{\cos^4(2\varphi)}{2}\right), \tag{24}$$

where $\sigma_0^{(3)} = \sigma_0^{(1)}(2ea\sqrt{2\pi}/\tau)^2$. A remarkable feature of the intraband conductivity in the third order is that, unlike the first

order, it is dependent on α and hence reveals some underlying geometry of the system.

Figure 5 shows that in the region where the intraband response is appreciable the dice lattice ($\alpha = 1$) is the superior nonlinear material, followed by the hybrid $\alpha = 0.5$ lattice then graphene. Physically, this implies that the flat band uniformly enhances the nonlinear intraband response.

The interband tensor contains all the harmonics of the system and is hence more complicated. Its simplest form is given by the 22-term sum

$$\begin{aligned}\frac{\mathrm{Re}\left(\sigma_x^{(3),\mathrm{inter}}\right)}{\sigma_0^{(3)}} &= \theta(3\hbar\omega-\mu)\frac{\tau^2\sin^2(2\varphi)}{\pi(\hbar\omega)^2}\left[\frac{3}{64}-\frac{\tau^2}{(\hbar\omega)^2}\left(\frac{27}{2048}+\frac{81\sin^2(2\varphi)}{2048}-\frac{1207\cos^2(2\varphi)}{17920}\right)\right]\\ &-\theta(3\hbar\omega-2\mu)\frac{\tau^2\cos^2(2\varphi)}{\pi(\hbar\omega)^2}\left[\frac{27}{2048}+\frac{\tau^2}{(\hbar\omega)^2}\left(\frac{27}{128}+\frac{81\sin^2(2\varphi)}{640}-\frac{81\cos^2(2\varphi)}{512}\right)\right]\\ &+\theta(2\hbar\omega-\mu)\frac{\tau^2\sin^2(2\varphi)}{\pi(\hbar\omega)^2}\left[\frac{1}{64}+\frac{\tau^2}{(\hbar\omega)^2}\left(\frac{3}{1024}-\frac{27\cos^2(2\varphi)}{320}\right)\right]\\ &-\theta(\hbar\omega-\mu)\frac{\tau^2}{\pi(\hbar\omega)^2}\left[\frac{3\sin^2(2\varphi)}{128}+\frac{\cos^2(2\varphi)}{128}+\frac{\tau^2}{(\hbar\omega)^2}\left(\begin{array}{l}\frac{3\sin^2(2\varphi)}{2048}-\frac{9\cos^2(2\varphi)}{64}+\frac{27\sin^4(2\varphi)}{2048}\\ +\frac{1467\sin^2(2\varphi)\cos^2(2\varphi)}{2560}+\frac{9\cos^4(2\varphi)}{128}\end{array}\right)\right]\\ &-\theta(\hbar\omega-2\mu)\frac{\tau^2\cos^2(2\varphi)}{\pi(\hbar\omega)^2}\left[\frac{3}{32}+\frac{\tau^2}{(\hbar\omega)^2}\left(\frac{9}{128}-\frac{27\sin^2(2\varphi)}{2240}-\frac{9\cos^2(2\varphi)}{512}\right)\right]. \qquad (25)\end{aligned}$$

Each Heaviside function in Eq. (25) represents the onset of a specific harmonic process. The processes are equated as per Table I. It should be noted that while a specific Heaviside function may represent the onset of a one- or two-photon process, it is always paired with another term in Eq. (25) to form a three-photon process.

Each one of these processes defines a distinct onset position as shown in Fig. 6. However, simply by inspection of Eq. (25) we note that the purely sin terms only contain flat-to-conduction band process terms. This agrees with the fact that when $\alpha = 1$ and all cos terms become 0, the valence band becomes inert. This is also the case for the other extremal value $\alpha = 0$ (where only the cos terms contribute) where, although the flat band is inert, the available energy states it provides enhances the third-order conductivity through the $\theta(\hbar\omega - \mu)$ terms. This enhancement is made possible since we consider multiple-photon processes.

It is also worth noting there are no 2ω intercone processes present. This is because the term $\theta(2\hbar\omega - 2\mu)$ defines a second-order time-reversal-invariant process, which gives no contribution to the conductivity since $\mathrm{Re}\,(\sigma_x^{(2)}) = 0$.

Critical physical information is plainly revealed by Fig. 6. For example, the higher magnitude peaks show the dominant harmonic process in each geometry. By noting that $\mu = 1$ meV corresponds to approximately to $\omega = 1.518$ THz, the dominant process for graphene is clearly identified as the single-photon valence-to-conduction band process (as

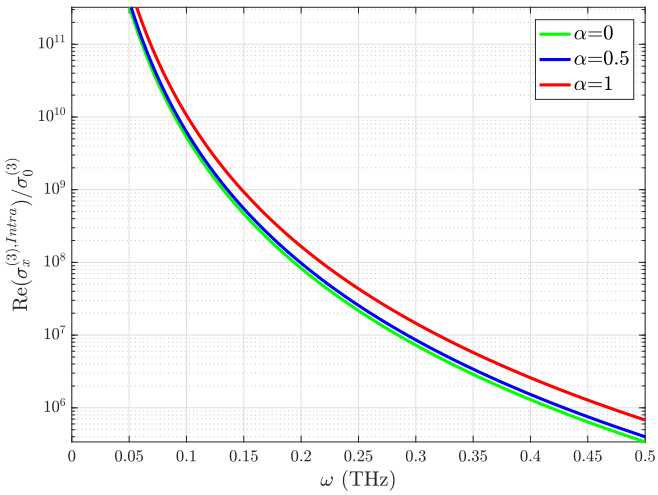

FIG. 5. Third-order intraband tensor component for $a = 0.0142$ nm, $\tau_1 = \tau_2 = 3$ eV, $\mu = 1$ meV, $\epsilon = 0$, and $T = 0$.

TABLE I. Third-order harmonic processes.

θ function	Onset of harmonic processes
$\theta(3\hbar\omega - \mu)$	Three-photon flat-to-conduction band
$\theta(\hbar\omega - \mu)$	One-photon flat-to-conduction band Paired with itself twice or Paired with a two-photon flat-to-conduction band to produce a three-photon flat-to-conduction band process
$\theta(\hbar\omega - 2\mu)$	One-photon valence-to-conduction band process Paired with itself twice to produce a three-photon valence-to-conduction band process
$\theta(2\hbar\omega - \mu)$	Two-photon flat-to-conduction band Paired with one-photon flat-to-conduction band to produce a three-photon flat-to-conduction band process
$\theta(3\hbar\omega - 2\mu)$	Three-photon valence-to-conduction band process

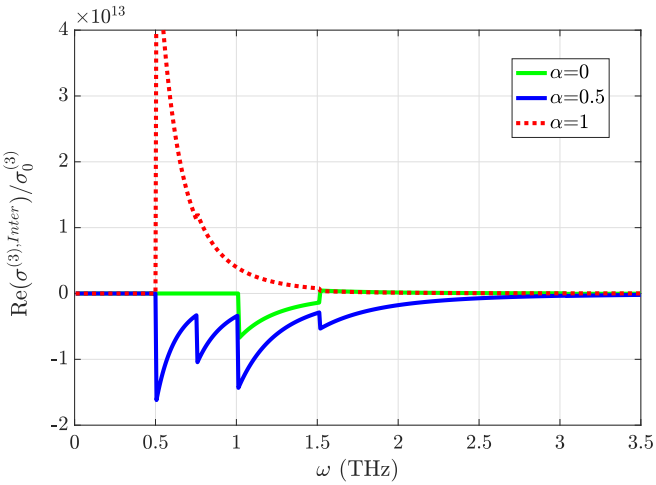

FIG. 6. Third-order interband tensor component as a function of ω for $a = 0.0142$ nm, $\tau_1 = \tau_2 = 3$ eV, $\mu = 1$ meV, $\epsilon = 0$, and $T = 0$.

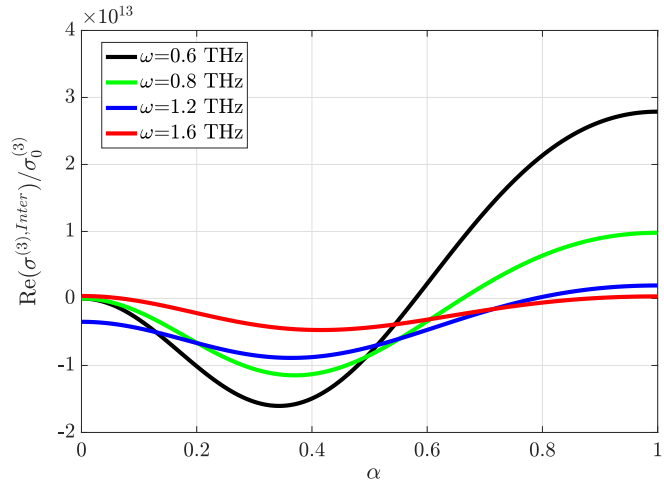

FIG. 7. Third-order interband tensor component as a function of α for $a = 0.0142$ nm, $\tau_1 = \tau_2 = 3$ eV, $\mu = 1$ meV, $\epsilon = 0$, and $T = 0$.

found in similar quantum frameworks [90,91,99]) whereas for $\alpha = 1$ the single-photon flat-to-conduction band process is dominant. The dominant contribution from the flat band is attributed to its high density of states compared to that of the valence band. This is because the rate of an optical transition is proportional to the joint density of states of the bands involved. Furthermore, for the third-order process, the rate is scaled by the inverse high powers of the transition energy. This further enhances the contribution of the flat band at low frequencies as shown in Fig. 6.

Second, the conductivity peaks decay with increased frequency due to the $(\hbar\omega)^{-n}$ terms, implying the first order will dominate at very high frequencies. This is discussed in the following subsection. We also note that the third-order conductivity is negative for some frequency intervals if $0 \leqslant \alpha < 1$. This does not imply a negative overall conductivity, instead a switching of signs for each odd-order conductivity term producing a smaller full nonlinear conductivity.

The existence of many distinct harmonics for certain lattice geometries is advantageous in applications that may require high-bandwidth modular nonlinear electronic devices. In such a setting one can use easily distinguishable fields to extract drastically different nonlinear behaviors out of a single material.

Figure 7 shows that the third-order conductivity has a clear trigonometric dependence on α, as expected since $\alpha = \tan(\varphi)$. The amplitude of the trigonometric curves, in general, decreases with applied field frequency as the $(\hbar\omega)^{-n}$ terms begin to dominate. These characteristics could, in practice, enable one to select an appropriate frequency for the geometry at hand, i.e., for $\alpha = 1$ one should use a lower-frequency field should they desire a larger magnitude nonlinear response. This is again outlined in the following subsection where the magnitude relative to the linear response becomes apparent.

C. Critical field

In nonlinear dynamics the critical field is described as the applied field required so that the first- and third-order currents have equal magnitude. Using Ohm's law it is found

$$\mathcal{E}_x^c = \sqrt{\left|\frac{\sigma_x^{(1)}}{\sigma_x^{(3)}}\right|}. \tag{26}$$

The critical field is plotted below as a function of frequency. Fig. 8 is the critical field determined by the total conductivity while Fig. 9 is the critical field determined by the intra-band conductivity only.

Since changing the chemical potential shifts the harmonics of both conductivities, changing μ will have the same effect on the critical field. Increasing the temperature results in a higher critical field. These phenomena have been predicted using more simplistic models for SLG in both quantum and classic regimes [90,99,100].

Furthermore, the magnitude of the critical field for any α value in the terahertz range is between 10^2–10^6 V/m. Previous models have predicted critical fields of the order 10^5–10^6 V/m [90,99,100]. Our results encompass this interval but

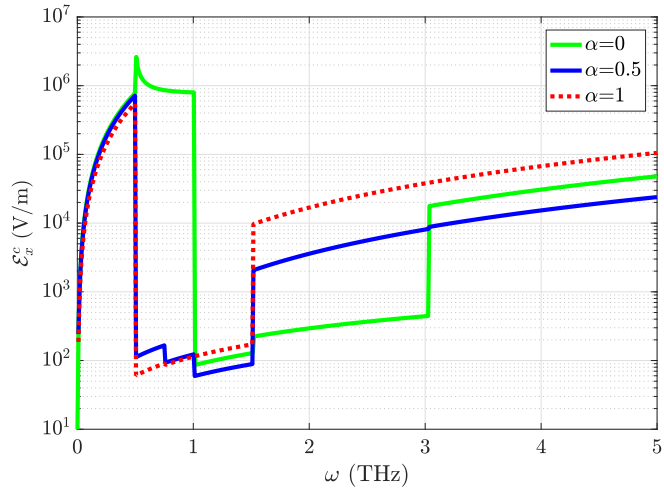

FIG. 8. Critical field for $a = 0.142$ nm, $\tau_1 = \tau_2 = 3$ eV, $\mu = 1$ meV, $\epsilon = 0$, and $T = 0$.

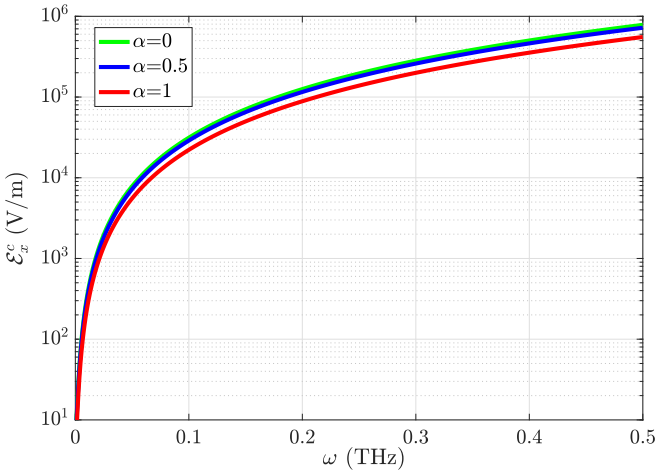

FIG. 9. Intraband response critical field for $a = 0.142$ nm, $\tau_1 = \tau_2 = 3$ eV, $\mu = 1$ meV, $\epsilon = 0$, and $T = 0$.

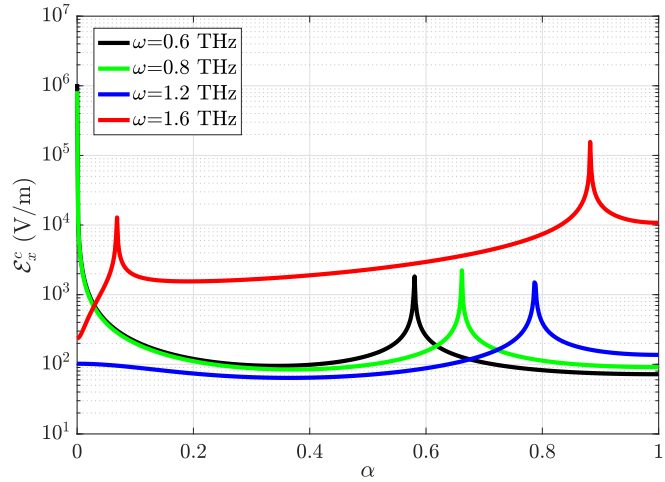

FIG. 10. α dependence on the critical field for $a = 0.142$ nm, $\tau_1 = \tau_2 = 3$ eV, $\mu = 1$ meV, $\epsilon = 0$, and $T = 0$.

reveal more interesting dynamics owing to the harmonics of the system. For example, each α value exhibits a region of small critical field; for $\alpha = 0$ this is between 0.5–1.5 THz, for $\alpha = 1$: 1–3 THz; and for $\alpha = 0.5$: 1001.5 THz. This is due to the first-order conductivity minimum in these regions while the dominant third-order harmonic process is present. These regions are practically desirable for high-efficiency photomixing and multiplying.

For higher terahertz fields ($\omega > 3.1$ THz) each critical field begins increasing with frequency at the same rate with $\mathcal{E}_x^c(\alpha = 0) > \mathcal{E}_x^c(\alpha = 1) > \mathcal{E}$. Mathematically, this is easy to see through the dominance of the $(\hbar\omega)^{-n}$ terms.

One of the striking properties we discussed in the previous section was the α dependence of the intraband response. By taking a closer look at the region $0 \leqslant \omega \leqslant 0.5$ THz, we explore what baring this phenomenon has on the critical field in Fig. 10.

As one can clearly observe by the small difference between the curves, the dependence of the intraband response on the underlying geometry of the system has little effect on the critical field. Although, similar to high-terahertz fields the ordering $\mathcal{E}_x^c(\alpha = 0) > \mathcal{E}_x^c(\alpha = 0.5) > \mathcal{E}_x^c(\alpha = 1)$ remains unchanged in this interval. Showing once again, the dice lattice will be the best nonlinear material at frequencies small enough for the intraband response to be appreciable.

Finally, we show the α dependence of the critical field at a number of applied frequency values. Each frequency curve shows an α-dependent set of characteristic peaks whereby the critical field increases rapidly by approximately an order of magnitude. These peaks occur when the frequency activates the dominant harmonic process for each lattice geometry, for example, $\alpha = 1$ would show a peak at $\omega = 0.5$ THz from Fig. 6. This information shows that, in practice, one could use the nonlinear dynamical response alone to efficiently characterize (measure α) an α-T_3-type lattice.

IV. SUMMARY AND CONCLUSIONS

Motivated by the importance of the nonlinear response associated with topological properties from the flat band in α-T_3 model, we have developed a second-quantized model capable of calculating the full nonlinear optical response (both intraband and interband) of an α-T_3 lattice. The first-, second-, and third-order dynamical conductivities have been calculated and investigated in depth.

First-order conductivity plots were produced for a number of α, chemical potential, and band-gap values as a function of frequency (Fig. 3). The results agree with previously established and accepted results [63], particularly the existence of frequency and α-dependent quantization if $\epsilon = 0$. Most notably, for the first order we reveal how a nonzero band gap can break the quantization of valence to conduction band transitions but leave flat band to conduction band transitions quantized. Meanwhile, the second-order conductivity was found to be 0, agreeing with the time-reversal invariance of the Hamiltonian and previously established results [63,90,99,100].

The previously unknown nonlinear dynamics of the α-T_3 model are revealed in the interband response. Although there is no quantization phenomenon in the third order, HHG is observed up to the third order. By equating the HHG with physical processes (see Table I) we also find that the flat band enhances both the intraband and interband conductivities. Furthermore, unlike the first-order conductivity, the intraband response is found to be dependent on α, revealing some underlying geometry of the system. This geometrical dependence of the intraband conductivity leads to the dice lattice being the superior nonlinear material for gigahertz frequencies and below. Finally, a trigonometric α dependence of the third-order conductivity is observed with lower-frequency fields being more heavily influenced by α due to the $(\hbar\omega)^{-n}$ terms.

Critical field calculations show values between 10^2–10^6 V/m, depending heavily on α and the applied field frequency (see Figs. 8 and 10). Due to the practically accessible critical field values, we conclude that α-T_3-type lattices may become practical for use as terahertz devices since the possibility to control the nonlinearity by an optical field is realized. Moreover, the characteristic peaks for each frequency give the possibility of characterizing the

geometry of the material based solely on the nonlinear dynamical response.

Our results show that the α-T_3 lattice exhibits a strong nonlinear response in the terahertz regime, similar to other topological materials [101]. Therefore, the effects discussed here should have useful applications in α-T_3-based devices. The strong $\sigma^{(3)}$ can lead to enhanced surface plasmon polariton excitation when α-T_3 is deposited on a dielectric substrate [102]. It can give rise to efficient frequency multiplication [103]. Such materials can also be used as a terahertz modulator with a large modulation depth under a field of around 10^4–10^5 V/m [104]. When the device is irradiated with two fields of different frequencies, the strong third-order effect can result in a higher-efficiency three-photon mixing.

ACKNOWLEDGMENT

This research has been supported by the Promoting the Connotative Development of Universities Project No. 21082718023, the Fundamental Research Fund of Beijing University of Civil Engineering and Architecture Grant No. X18176, the Australian Research Council grant (Grant No. DP160101474), NSFC (Grant No. 11774006), and NBRP of China (Grant No. 2012CB921300).

APPENDIX A: SECOND- AND THIRD-ORDER REDUCED DENSITY MATRICES

The probabilities of a single charge carrier coupling to two photons are determined by the following reduced density matrix components:

$$\rho^{(2)}_{0,0}(\mathbf{k},\omega)=\sum_{\lambda}\left|M^{(1)}_{\lambda,0}\right|^2\frac{(n_0-n_\lambda)}{(\hbar\omega)^2-E_\lambda^2}, \tag{A1}$$

$$\rho^{(2)}_{\lambda,0}(\mathbf{k},\omega)=\left[M^{(2)}_{0,\lambda}-\frac{M^{(1)}_{\lambda,\lambda}M^{(1)}_{0,\lambda}}{\hbar\omega+E_\lambda}\right]\frac{n_\lambda-n_0}{2\hbar\omega+E_\lambda}+\frac{M^{(1)}_{-\lambda,\lambda}M^{(1)}_{0,-\lambda}}{\hbar\omega+E_{-\lambda}}\frac{n_0-n_{-\lambda}}{2\hbar\omega+E_\lambda}+\frac{M^{(1)}_{-\lambda,\lambda}M^{(1)}_{0,-\lambda}}{\hbar\omega+E_\lambda-E_{-\lambda}}\frac{n_\lambda-n_{-\lambda}}{2\hbar\omega+E_\lambda}, \tag{A2}$$

$$\rho^{(2)}_{0,\lambda}(\mathbf{k},\omega)=\left[M^{(2)}_{\lambda,0}+\frac{M^{(1)}_{\lambda,\lambda}M^{(1)}_{\lambda,0}}{\hbar\omega-E_\lambda}\right]\frac{n_0-n_\lambda}{2\hbar\omega-E_\lambda}+\frac{M^{(1)}_{\lambda,-\lambda}M^{(1)}_{-\lambda,0}}{\hbar\omega-E_{-\lambda}}\frac{n_0-n_{-\lambda}}{2\hbar\omega-E_\lambda}+\frac{M^{(1)}_{\lambda,-\lambda}M^{(1)}_{-\lambda,0}}{\hbar\omega+E_{-\lambda}-E_\lambda}\frac{n_\lambda-n_{-\lambda}}{2\hbar\omega-E_\lambda}, \tag{A3}$$

$$\rho^{(2)}_{\lambda,\lambda}(\mathbf{k},\omega)=\left|M^{(1)}_{\lambda,0}\right|^2\frac{n_\lambda-n_0}{(\hbar\omega)^2-E_\lambda^2}+\left|M^{(1)}_{\lambda,-\lambda}\right|^2\frac{n_\lambda-n_{-\lambda}}{(\hbar\omega)^2-(E_\lambda-E_{-\lambda})^2}, \tag{A4}$$

$$\rho^{(2)}_{\lambda,-\lambda}(\mathbf{k},\omega)=\frac{M^{(1)}_{-\lambda,0}M^{(1)}_{0,\lambda}}{2\hbar\omega+E_\lambda-E_{-\lambda}}\left[\frac{n_\lambda-n_0}{\hbar\omega+E_\lambda}+\frac{n_{-\lambda}-n_0}{\hbar\omega-E_{-\lambda}}\right]+\left[M^{(2)}_{-\lambda,\lambda}-\frac{M^{(1)}_{-\lambda,\lambda}\left(M^{(1)}_{\lambda,\lambda}-M^{(1)}_{-\lambda,-\lambda}\right)}{\hbar\omega+(E_\lambda-E_{-\lambda})}\right]\frac{n_\lambda-n_{-\lambda}}{2\hbar\omega+E_\lambda-E_{-\lambda}}. \tag{A5}$$

When combined with the first-order components [(13) and (14)], all components proportional to A_ω^2 appearing in Eq. (15) will cancel out. For example, consider the component $\propto A_\omega^2$ in (15) with $\epsilon=0$, $n=2$, and $m=1$:

$$\begin{aligned}c\sum_{\mathbf{k},\lambda}2A_\omega^2\left(M^{(2)}_{\lambda,0}\rho^{(1)}_{\lambda,0}+M^{(2)}_{0,\lambda}\rho^{(1)}_{0,\lambda}\right)&=2c\sum_{\mathbf{k},\lambda}A_\omega^2\left(-\frac{M^{(2)}_{\lambda,0}M^{(1)}_{0,\lambda}}{\hbar\omega+E_\lambda}-\frac{M^{(2)}_{0,\lambda}M^{(1)}_{\lambda,0}}{\hbar\omega-E_\lambda}\right)\\&=2c\sum_{\lambda}A_\omega^2\sum_{\mathbf{k}}\mathcal{M}(\mathbf{k})(n_0-n_\lambda)\left[\frac{1}{\hbar\omega-E_\lambda}+\frac{1}{\hbar\omega+E_\lambda}\right],\end{aligned}$$

where

$$\mathcal{M}(\mathbf{k})=\tau^2\left(\frac{\sqrt{3}ea}{2\hbar c}\right)^3\sin^2(2\varphi)\cos\left(\frac{\sqrt{3}}{2}k_xa\right)\sin\left(\frac{\sqrt{3}}{2}k_xa\right)\sin^2\left(\frac{3}{2}K_ya\right).$$

Now, since $\mathcal{M}(\mathbf{k})=-\mathcal{M}(-\mathbf{k})$, $E_\lambda(\mathbf{k})=E_\lambda(-\mathbf{k})$, and $n_\lambda(\mathbf{k})=n_\lambda(-\mathbf{k})$, the summand is symmetric in $\mathbf{k}$ so summing over $\mathbf{k}$ yields

$$c\sum_{\mathbf{k},\lambda}2A_\omega^2\left(M^{(2)}_{\lambda,0}\rho^{(1)}_{\lambda,0}+M^{(2)}_{0,\lambda}\rho^{(1)}_{0,\lambda}\right)=0.$$

This is how we arrive at $\mathrm{Re}(\sigma^{(2)})=0$.

The highest-order photon process we consider is the third order. The probabilities of a single charge carrier coupling to three photons are determined by the following reduced density matrix components:

$$\begin{aligned}
&\rho^{(3)}_{0,0}(\mathbf{k},\omega)\\
&= \frac{1}{3\hbar\omega}\sum_{\lambda}\left|M^{(1)}_{\lambda,0}\right|^2 M^{(1)}_{\lambda,\lambda}\left[\frac{1}{(\hbar\omega-E_\lambda)(2\hbar\omega-E_\lambda)}-\frac{1}{(\hbar\omega-E_\lambda)(2\hbar\omega-E_\lambda)}\right](n_0-n_\lambda)\\
&\quad+\frac{1}{3\hbar\omega}\sum_{\lambda}\left[\frac{\left(M^{(1)}_{-\lambda,\lambda}M^{(1)}_{0,-\lambda}M^{(1)}_{\lambda,0}\right)^*}{(\hbar\omega-E_{-\lambda})(2\hbar\omega-E_\lambda)}-\frac{M^{(1)}_{-\lambda,\lambda}M^{(1)}_{0,-\lambda}M^{(1)}_{\lambda,0}}{(\hbar\omega+E_{-\lambda})(2\hbar\omega+E_\lambda)}\right](n_0-n_{-\lambda})\\
&\quad+\frac{1}{3\hbar\omega}\sum_{\lambda}\left[\frac{\left(M^{(1)}_{0,-\lambda}M^{(1)}_{-\lambda,\lambda}M^{(1)}_{\lambda,0}\right)^*}{(\hbar\omega-E_\lambda+E_{-\lambda})(2\hbar\omega-E_\lambda)}-\frac{M^{(1)}_{0,-\lambda}M^{(1)}_{-\lambda,\lambda}M^{(1)}_{\lambda,0}}{(\hbar\omega+E_\lambda-E_{-\lambda})(2\hbar\omega+E_\lambda)}\right](n_\lambda-n_{-\lambda})\\
&\quad+\sum_{\lambda}\left[\frac{\left(M^{(2)}_{0,\lambda}M^{(1)}_{\lambda,0}\right)^*}{(2\hbar\omega-E_\lambda)(\hbar\omega+E_\lambda)}+\frac{M^{(2)}_{0,\lambda}M^{(1)}_{\lambda,0}}{(2\hbar\omega+E_\lambda)(\hbar\omega-E_\lambda)}\right](n_0-n_\lambda),
\end{aligned}\tag{A6}$$

$$\begin{aligned}
&\rho^{(3)}_{\lambda,0}(\mathbf{k},\omega)\\
&=\frac{M^{(3)}_{0,-\lambda}n_{-\lambda}-M^{(3)}_{0,\lambda}(n_0-n_\lambda)}{3\hbar\omega+E_\lambda}\\
&\quad+\frac{(n_0-n_\lambda)}{3\hbar\omega+E_\lambda}\left[\frac{M^{(1)}_{\lambda,\lambda}M^{(2)}_{0,\lambda}}{2\hbar\omega+E_\lambda}+\frac{M^{(2)}_{\lambda,\lambda}M^{(1)}_{0,\lambda}}{\hbar\omega+E_\lambda}\right]+\frac{(n_0-n_{-\lambda})}{3\hbar\omega+E_\lambda}\left[\frac{M^{(1)}_{-\lambda,\lambda}M^{(2)}_{0,-\lambda}}{2\hbar\omega+E_{-\lambda}}+\frac{M^{(2)}_{-\lambda,\lambda}M^{(1)}_{0,-\lambda}}{\hbar\omega+E_{-\lambda}}\right]\\
&\quad-\frac{(n_0-n_\lambda)}{3\hbar\omega+E_\lambda}\left[\frac{\left|M^{(1)}_{\lambda,\lambda}\right|^2M^{(1)}_{0,\lambda}}{(2\hbar\omega+E_\lambda)(\hbar\omega+E_\lambda)}+\frac{\left|M^{(1)}_{-\lambda,\lambda}\right|^2M^{(1)}_{0,\lambda}}{(2\hbar\omega+E_{-\lambda})(\hbar\omega+E_\lambda)}+\frac{2\left|M^{(1)}_{0,\lambda}\right|^2M^{(1)}_{0,\lambda}}{(\hbar\omega)^2-E_\lambda^2}\right]\\
&\quad-\frac{(n_0-n_{-\lambda})}{3\hbar\omega+E_\lambda}\left[\frac{M^{(1)}_{\lambda,\lambda}M^{(1)}_{-\lambda,\lambda}M^{(1)}_{0,-\lambda}}{(2\hbar\omega+E_\lambda)(\hbar\omega+E_{-\lambda})}+\frac{M^{(1)}_{-\lambda,-\lambda}M^{(1)}_{-\lambda,\lambda}M^{(1)}_{0,\lambda}}{(2\hbar\omega+E_{-\lambda})(\hbar\omega+E_{-\lambda})}+\frac{\left|M^{(1)}_{0,-\lambda}\right|^2\left(M^{(1)}_{0,\lambda}+M^{(1)}_{0,-\lambda}\right)}{(\hbar\omega)^2-(E_{-\lambda})^2}\right]\\
&\quad-\frac{(n_\lambda-n_{-\lambda})}{3\hbar\omega+E_\lambda}\left[\frac{M^{(1)}_{\lambda,\lambda}M^{(1)}_{-\lambda,\lambda}M^{(1)}_{0,-\lambda}}{(2\hbar\omega+E_\lambda)(\hbar\omega+E_\lambda-E_{-\lambda})}-\frac{\left|M^{(1)}_{\lambda,-\lambda}\right|^2M^{(1)}_{0,\lambda}}{(2\hbar\omega+E_{-\lambda})(\hbar\omega+E_{-\lambda}-E_\lambda)}-\frac{\left|M^{(1)}_{\lambda,-\lambda}\right|^2\left(M^{(1)}_{0,\lambda}-M^{(1)}_{0,-\lambda}\right)}{(\hbar\omega)^2-(E_\lambda-E_{-\lambda})^2}\right],
\end{aligned}\tag{A7}$$

$$\begin{aligned}
&\rho^{(3)}_{0,\lambda}(\mathbf{k},\omega)\\
&=-\frac{M^{(3)}_{-\lambda,0}n_{-\lambda}-M^{(3)}_{\lambda,0}(n_0-n_\lambda)}{3\hbar\omega-E_\lambda}\\
&\quad+\frac{(n_0-n_\lambda)}{3\hbar\omega-E_\lambda}\left[\frac{M^{(1)}_{\lambda,\lambda}M^{(2)}_{\lambda,0}}{2\hbar\omega-E_\lambda}+\frac{M^{(2)}_{\lambda,\lambda}M^{(1)}_{\lambda,0}}{\hbar\omega-E_\lambda}\right]+\frac{(n_0-n_{-\lambda})}{3\hbar\omega-E_\lambda}\left[\frac{M^{(1)}_{\lambda,-\lambda}M^{(2)}_{-\lambda,0}}{2\hbar\omega-E_{-\lambda}}+\frac{M^{(2)}_{\lambda,-\lambda}M^{(1)}_{-\lambda,0}}{\hbar\omega-E_{-\lambda}}\right]\\
&\quad+\frac{(n_0-n_\lambda)}{3\hbar\omega-E_\lambda}\left[\frac{\left|M^{(1)}_{\lambda,\lambda}\right|^2M^{(1)}_{\lambda,0}}{(2\hbar\omega-E_\lambda)(\hbar\omega-E_\lambda)}+\frac{\left|M^{(1)}_{\lambda,-\lambda}\right|^2M^{(1)}_{\lambda,0}}{(2\hbar\omega-E_\lambda)(\hbar\omega-E_{-\lambda})}+\frac{2\left|M^{(1)}_{\lambda,0}\right|^2M^{(1)}_{\lambda,0}}{(\hbar\omega)^2-E_\lambda^2}\right]\\
&\quad+\frac{(n_0-n_{-\lambda})}{3\hbar\omega-E_\lambda}\left[\frac{M^{(1)}_{\lambda,\lambda}M^{(1)}_{-\lambda,-\lambda}M^{(1)}_{-\lambda,0}}{(2\hbar\omega-E_\lambda)(\hbar\omega-E_{-\lambda})}+\frac{M^{(1)}_{-\lambda,-\lambda}M^{(1)}_{\lambda,-\lambda}M^{(1)}_{\lambda,0}}{(2\hbar\omega-E_{-\lambda})(\hbar\omega-E_{-\lambda})}+\frac{\left|M^{(1)}_{-\lambda,0}\right|^2\left(M^{(1)}_{\lambda,0}+M^{(1)}_{-\lambda,0}\right)}{(\hbar\omega)^2-(E_{-\lambda})^2}\right]\\
&\quad-\frac{(n_\lambda-n_{-\lambda})}{3\hbar\omega-E_\lambda}\left[\frac{M^{(1)}_{\lambda,\lambda}M^{(1)}_{-\lambda,0}M^{(1)}_{\lambda,-\lambda}}{(2\hbar\omega-E_\lambda)(\hbar\omega-E_\lambda+E_{-\lambda})}-\frac{\left|M^{(1)}_{\lambda,-\lambda}\right|^2M^{(1)}_{\lambda,0}}{(2\hbar\omega-E_{-\lambda})(\hbar\omega-E_{-\lambda}+E_\lambda)}-\frac{\left|M^{(1)}_{\lambda,-\lambda}\right|^2\left(M^{(1)}_{\lambda,0}-M^{(1)}_{-\lambda,0}\right)}{(\hbar\omega)^2-(E_\lambda-E_{-\lambda})^2}\right],
\end{aligned}\tag{A8}$$

$$\rho^{(3)}_{\lambda,\lambda}(\mathbf{k},\omega)$$

$$= \frac{1}{3\hbar\omega}\left(\frac{M^{(1)}_{\lambda,0}M^{(1)}_{0,-\lambda}M^{(1)}_{-\lambda,\lambda}}{2\hbar\omega - E_\lambda + E_{-\lambda}}\left[\frac{n_0-n_{-\lambda}}{\hbar\omega+E_{-\lambda}}+\frac{n_0-n_\lambda}{\hbar\omega-E_\lambda}\right] - \frac{\left(M^{(1)}_{\lambda,0}M^{(1)}_{0,-\lambda}M^{(1)}_{-\lambda,\lambda}\right)^*}{2\hbar\omega + E_\lambda - E_{-\lambda}}\left[\frac{n_0-n_\lambda}{\hbar\omega+E_\lambda}+\frac{n_0-n_{-\lambda}}{\hbar\omega-E_{-\lambda}}\right]\right)$$

$$+ \frac{(n_0-n_\lambda)}{3\hbar\omega}\left[\frac{\left|M^{(1)}_{0,\lambda}\right|^2 M^{(1)}_{\lambda,\lambda}}{(\hbar\omega+E_\lambda)(2\hbar\omega+E_\lambda)} - \frac{\left|M^{(1)}_{0,\lambda}\right|^2 M^{(1)}_{\lambda,\lambda}}{(\hbar\omega-E_\lambda)(2\hbar\omega-E_\lambda)}\right]$$

$$- (n_0-n_\lambda)\left[\frac{M^{(2)}_{0,\lambda}M^{(1)}_{\lambda,0}}{(\hbar\omega-E_\lambda)(2\hbar\omega+E_\lambda)} + \frac{\left(M^{(2)}_{0,\lambda}M^{(1)}_{\lambda,0}\right)^*}{(\hbar\omega-E_\lambda)(2\hbar\omega-E_\lambda)}\right]$$

$$+ \frac{(n_0-n_{-\lambda})}{3\hbar\omega}\left[\frac{M^{(1)}_{-\lambda,\lambda}M^{(1)}_{0,-\lambda}M^{(1)}_{\lambda,0}}{(\hbar\omega+E_{-\lambda})(2\hbar\omega+E_\lambda)} - \frac{\left(M^{(1)}_{-\lambda,\lambda}M^{(1)}_{0,-\lambda}M^{(1)}_{\lambda,0}\right)^*}{(\hbar\omega-E_\lambda)(2\hbar\omega-E_\lambda)}\right]$$

$$+ \frac{(n_\lambda-n_{-\lambda})}{3\hbar\omega}\left[\frac{M^{(1)}_{0,-\lambda}M^{(1)}_{-\lambda,\lambda}M^{(1)}_{\lambda,0}}{(\hbar\omega+E_\lambda-E_{-\lambda})(2\hbar\omega+E_\lambda)} - \frac{\left(M^{(1)}_{0,-\lambda}M^{(1)}_{-\lambda,\lambda}M^{(1)}_{\lambda,0}\right)^*}{(\hbar\omega+E_{-\lambda}-E_\lambda)(2\hbar\omega-E_\lambda)}\right]$$

$$- \frac{(n_\lambda-n_{-\lambda})}{3\hbar\omega}\left[\frac{M^{(1)}_{\lambda,-\lambda}\left(M^{(1)}_{-\lambda,-\lambda}-M^{(1)}_{\lambda,\lambda}\right)}{(2\hbar\omega+E_{-\lambda}-E_\lambda)(\hbar\omega+E_{-\lambda}-E_\lambda)} - \frac{\left(M^{(1)}_{\lambda,-\lambda}\right)^*\left(M^{(1)}_{-\lambda,-\lambda}-M^{(1)}_{\lambda,\lambda}\right)}{(2\hbar\omega+E_\lambda-E_{-\lambda})(\hbar\omega+E_\lambda-E_{-\lambda})}\right]$$

$$+ (n_\lambda-n_{-\lambda})\left[\frac{M^{(2)}_{\lambda,-\lambda}M^{(1)}_{-\lambda,\lambda}}{(2\hbar\omega+E_{-\lambda}-E_\lambda)(\hbar\omega+E_\lambda-E_{-\lambda})} + \frac{\left(M^{(2)}_{\lambda,-\lambda}M^{(1)}_{-\lambda,\lambda}\right)^*}{(2\hbar\omega+E_\lambda-E_{-\lambda})(\hbar\omega+E_{-\lambda}-E_\lambda)}\right], \tag{A9}$$

$$\rho^{(3)}_{\lambda,-\lambda}(\mathbf{k},\omega)$$

$$= -\frac{1}{3\hbar\omega+E_\lambda-E_{-\lambda}}\left(M^{(2)}_{-\lambda,0}M^{(1)}_{0,\lambda}\left[\frac{n_0-n_\lambda}{\hbar\omega+E_\lambda}+\frac{n_0-n_{-\lambda}}{2\hbar\omega-E_{-\lambda}}\right] + M^{(2)}_{0,-\lambda}M^{(1)}_{-\lambda,0}\left[\frac{n_0-n_\lambda}{2\hbar\omega+E_\lambda}+\frac{n_0-n_{-\lambda}}{\hbar\omega-E_{-\lambda}}\right]\right.$$

$$\left. - \frac{M^{(1)}_{-\lambda,0}M^{(1)}_{0,\lambda}\left(M^{(1)}_{\lambda,\lambda}-M^{(1)}_{-\lambda,-\lambda}\right)}{2\hbar\omega+E_\lambda-E_{-\lambda}}\left[\frac{n_0-n_\lambda}{\hbar\omega+E_\lambda}+\frac{n_0-n_{-\lambda}}{\hbar\omega-E_{-\lambda}}\right]\right)$$

$$+ \frac{M^{(1)}_{-\lambda,\lambda}\left(M^{(1)}_{\lambda,\lambda}-M^{(1)}_{-\lambda,-\lambda}\right)^2(n_\lambda-n_{-\lambda})}{(3\hbar\omega+E_\lambda-E_{-\lambda})(2\hbar\omega+E_\lambda-E_{-\lambda})(\hbar\omega+E_\lambda-E_{-\lambda})}$$

$$\frac{n_\lambda-n_{-\lambda}}{3\hbar\omega+E_\lambda-E_{-\lambda}}\left[M^{(3)}_{-\lambda,\lambda} - \frac{M^{(2)}_{-\lambda,\lambda}\left(M^{(1)}_{\lambda,\lambda}-M^{(1)}_{-\lambda,-\lambda}\right)}{2\hbar\omega+E_\lambda-E_{-\lambda}} - \frac{M^{(1)}_{-\lambda,\lambda}\left(M^{(2)}_{\lambda,\lambda}-M^{(2)}_{-\lambda,-\lambda}\right)}{\hbar\omega+E_\lambda-E_{-\lambda}}\right]$$

$$+ \frac{n_0-n_\lambda}{3\hbar\omega+E_\lambda-E_{-\lambda}}\left[\frac{M^{(1)}_{0,\lambda}M^{(1)}_{-\lambda,0}M^{(1)}_{-\lambda,-\lambda}}{(2\hbar\omega+E_\lambda)(\hbar\omega+E_\lambda)} - \frac{\left|M^{(1)}_{0,\lambda}\right|^2 M^{(1)}_{-\lambda,\lambda}}{(2\hbar\omega-E_{-\lambda})(\hbar\omega-E_\lambda)} - \frac{\left|M^{(1)}_{0,\lambda}\right|^2 M^{(1)}_{-\lambda,\lambda}}{(\hbar\omega)^2-E_\lambda^2}\right]$$

$$+ \frac{n_0-n_{-\lambda}}{3\hbar\omega+E_\lambda-E_{-\lambda}}\left[\frac{\left|M^{(1)}_{-\lambda,0}\right|^2 M^{(1)}_{-\lambda,\lambda}}{(2\hbar\omega+E_\lambda)(\hbar\omega+E_{-\lambda})} - \frac{M^{(1)}_{0,\lambda}M^{(1)}_{-\lambda,\lambda}M^{(1)}_{-\lambda,0}}{(2\hbar\omega-E_{-\lambda})(\hbar\omega-E_{-\lambda})} + \frac{\left|M^{(1)}_{-\lambda,0}\right|^2 M^{(1)}_{-\lambda,\lambda}}{(\hbar\omega)^2-E_{-\lambda}^2}\right]$$

$$+ \frac{n_\lambda-n_{-\lambda}}{3\hbar\omega+E_\lambda-E_{-\lambda}}\left[\frac{\left|M^{(1)}_{-\lambda,0}\right|^2 M^{(1)}_{-\lambda,\lambda}}{(2\hbar\omega+E_\lambda)(\hbar\omega+E_{-\lambda}-E_{-\lambda})} + \frac{\left|M^{(1)}_{0,\lambda}\right|^2 M^{(1)}_{-\lambda,\lambda}}{(2\hbar\omega-E_{-\lambda})(\hbar\omega+E_\lambda-E_{-\lambda})} + \frac{\left|M^{(1)}_{-\lambda,\lambda}\right|^2 M^{(1)}_{-\lambda,\lambda}}{(\hbar\omega)^2-(E_\lambda-E_{-\lambda})^2}\right]. \tag{A10}$$

APPENDIX B: FULL NONLINEAR THIRD-ORDER CONDUCTIVITY TENSOR COMPONENTS

Without using a linear approximation to the dispersion, one can obtain the full nonlinear third-order conductivity tensor terms, just as in the linear case. The intraband contribution is

$$\frac{\mathrm{Re}\left(\sigma_x^{(3),\mathrm{intra}}\right)}{\sigma_0^{(3)}} = \left(\frac{3a\tau\pi}{2}\right)^2 (n_+ - n_-)\delta^3(\hbar\omega) \sum_{k,\lambda} \left\{ \frac{\cos^2(2\varphi)}{2} \frac{\Lambda'''(\mathbf{k})}{|f_\mathbf{k}|^3} - \frac{1}{\tau}\frac{\Lambda(\mathbf{k})^2}{|f_\mathbf{k}|^3}\left(\sin^4(2\varphi) + \frac{\sin^2(2\varphi)\cos^2(2\varphi)}{2} + \frac{\cos^4(2\varphi)}{2}\right) \right.$$
$$\left. + \tau\left(\frac{1}{48}\Lambda^{\mathrm{IV}}(\mathbf{k}) - \frac{1}{24}\frac{\Lambda(\mathbf{k})}{|f_\mathbf{k}|} + \frac{1}{8}\frac{\Lambda''(\mathbf{k})}{|f_\mathbf{k}|} - \frac{5}{4}\frac{\Lambda'''(\mathbf{k})}{|f_\mathbf{k}|^2} - \frac{\sin^2(2\varphi)}{4}\frac{\Lambda'''(\mathbf{k})}{|f_\mathbf{k}|^2}\right)\right\}, \tag{B1}$$

where the Λ terms are given by

$$\Lambda''(\mathbf{k}) = \cos^2\left(\frac{\sqrt{3}}{2}k_x a\right)\sin^2\left(\frac{3}{2}K_y a\right), \tag{B2}$$

$$\Lambda'''(\mathbf{k}) = \sin^2\left(\frac{\sqrt{3}}{2}k_x a\right)\cos\left(\frac{\sqrt{3}}{2}k_x a\right)\sin^2\left(\frac{3}{2}K_y a\right)\cos\left(\frac{3}{2}K_y a\right), \tag{B3}$$

and

$$\Lambda^{\mathrm{IV}}(\mathbf{k}) = \cos\left(\frac{\sqrt{3}}{2}k_x a\right)\cos\left(\frac{3}{2}K_y a\right). \tag{B4}$$

The interband contribution is

$$\frac{\mathrm{Re}\left(\sigma_x^{(3),\mathrm{inter}}\right)}{\sigma_0^{(3)}} = \left(\frac{3a\tau}{2}\right)^2 (n_+ - n_-)$$
$$\times \sum_{k,\lambda}\left\{ \delta(3\hbar\omega + E_\lambda)\frac{\tau\sin^2(2\varphi)}{(\hbar\omega)^2|f_\mathbf{k}|}\left[-\frac{\Lambda(\mathbf{k})}{8} + \frac{\tau^2}{(\hbar\omega)^2}\left(\frac{3\Lambda^V(\mathbf{k})^2}{16} + \frac{1207\cos^2(2\varphi)\Lambda(\mathbf{k})^2}{3780} - \frac{3\sin^2(2\varphi)\Lambda(\mathbf{k})^2}{16}\right)\right]\right.$$
$$+ \delta(3\hbar\omega + 2E_\lambda)\frac{\tau\cos^2(2\varphi)}{(\hbar\omega)^2|f_\mathbf{k}|}\left[\frac{3\Lambda(\mathbf{k})^2}{16} - \frac{33\lambda\tau\Lambda'''(\mathbf{k})}{24(\hbar\omega)} + \frac{\tau^2}{(\hbar\omega)^2}\left(3\Lambda^V(\mathbf{k})^2 - \frac{3\cos^2(2\varphi)\Lambda(\mathbf{k})^2}{4} + \frac{3\sin^2(2\varphi)\Lambda(\mathbf{k})^2}{20}\right)\right]$$
$$- \delta(2\hbar\omega + E_\lambda)\frac{\tau\sin^2(2\varphi)}{(\hbar\omega)^2|f_\mathbf{k}|}\left[\frac{\Lambda''(\mathbf{k})}{8} + \frac{\lambda\tau\Lambda'''(\mathbf{k})}{2(\hbar\omega)} - \frac{\tau^2}{(\hbar\omega)^2}\left(\frac{2\cos^2(2\varphi)\Lambda(\mathbf{k})^2}{5} - \frac{\Lambda^{\mathrm{V}}(\mathbf{k})^2}{24}\right)\right]$$
$$+ \delta(\hbar\omega + E_\lambda)\frac{\tau}{(\hbar\omega)^2|f_\mathbf{k}|}\left(\begin{array}{c}\frac{\sin^2(2\varphi)\Lambda(\mathbf{k})}{16} + \frac{\cos^2(2\varphi)\Lambda''(\mathbf{k})}{16} + \frac{\lambda\tau\Lambda'''(\mathbf{k})}{(\hbar\omega)}\left(\frac{\sin^2(2\varphi)}{8} + \frac{11\cos^2(2\varphi)}{24}\right) \\ + \frac{\tau^2}{(\hbar\omega)^2}\left(\frac{\sin^2(2\varphi)\Lambda(\mathbf{k})^2}{16} + \frac{163\sin^2(2\varphi)\cos^2(2\varphi)\Lambda(\mathbf{k})^2}{60} + \frac{\cos^2(2\varphi)\Lambda(\mathbf{k})^2}{3} + \frac{\sin^2(2\varphi)\Lambda^{\mathrm{V}}(\mathbf{k})^2}{48} - \cos^2(2\varphi)\Lambda^{\mathrm{V}}(\mathbf{k})^2\right)\end{array}\right)$$
$$\left. + \delta(\hbar\omega + E_\lambda)\frac{\tau}{(\hbar\omega)^2|f_\mathbf{k}|}\left(\begin{array}{c}\frac{\cos^2(2\varphi)\Lambda(\mathbf{k})}{4} - \frac{\lambda\tau\Lambda'''(\mathbf{k})}{(\hbar\omega)}\left(\frac{\sin^2(2\varphi)}{4} + \frac{13\cos^2(2\varphi)}{24}\right) \\ + \frac{\tau^2}{(\hbar\omega)^2}\left(\frac{2\sin^2(2\varphi)\cos^2(2\varphi)\Lambda(\mathbf{k})^2}{35} - \frac{\cos^4(2\varphi)\Lambda(\mathbf{k})^2}{12} + \cos^2(2\varphi)\Lambda^{\mathrm{V}}(\mathbf{k})^2\right)\end{array}\right)\right\}, \tag{B5}$$

where

$$\Lambda^{\mathrm{V}}(\mathbf{k}) = \sin^2\left(\frac{\sqrt{3}}{2}k_x a\right)\sin\left(\frac{3}{2}K_y a\right)\cos\left(\frac{3}{2}K_y a\right). \tag{B6}$$

Results for the third-order conductivity using the full nonlinear dispersion, coincide with Fig. 6, once again highlighting the suitability of a linear approximation to the dispersion when $\epsilon = 0$ in the terahertz regime. Physically, this is because most of the charge carriers reside near the Dirac point.

[1] K. S. Novoselov, A. K. Geim, S. V. Morozov, D. Jiang, Y. Zhang, S. V. Dubonos, I. V. Grigorieva, and A. A. Firsov, Science **306**, 666 (2004).

[2] K. S. Novoselov, A. K. Geim, S. V. Morozov, D. Jiang, M. I. Katsnelson, I. V. Grigorieva, S. V. Dubonos, and A. A. Firsov, Nature (London) **438**, 197 (2005).

[3] M. I. Katsnelson, K. S. Novoselov, and A. K. Geim, Nat. Phys. **2**, 620 (2006).

[4] A. H. Castro Neto, F. Guinea, N. M. R. Peres, K. S. Novoselov, and A. K. Geim, Rev. Mod. Phys. **81**, 109 (2009).

[5] N. M. R. Peres, Rev. Mod. Phys. **82**, 2673 (2010).

[6] S. Das Sarma, S. Adam, E. H. Hwang, and E. Rossi, Rev. Mod. Phys. **83**, 407 (2011).
[7] M. Z. Hasan and C. L. Kane, Rev. Mod. Phys. **82**, 3045 (2010).
[8] X.-L. Qi and S.-C. Zhang, Rev. Mod. Phys. **83**, 1057 (2011).
[9] X. Wan, A. M. Turner, A. Vishwanath, and S. Y. Savrasov, Phys. Rev. B **83**, 205101 (2011).
[10] T. T. Heikkilä and G. E. Volovik, Pisma Zh. Eksp. Teor. Fiz. **93**, 63 (2011) [JETP Lett. **93**, 59 (2011)].
[11] A. A. Burkov, M. D. Hook, and L. Balents, Phys. Rev. B **84**, 235126 (2011).
[12] L. M. Schoop, M. N. Ali, C. Straßer, A. Topp, A. Varykhalov, D. Marchenko, V. Duppel, S. S. P. Parkin, B. V. Lotsch, and C. R. Ast, Nat. Commun. **7**, 11696 (2016).
[13] D. Takane, K. Nakayama, S. Souma, T. Wada, Y. Okamoto, K. Takenaka, Y. Yamakawa, A. Yamakage, T. Mitsuhashi, K. Horiba, H. Kumigashira, T. Takahashi, and T. Sato, npj Quantum Mater. **3**, 1 (2018).
[14] G. W. Semenoff, Phys. Rev. Lett. **53**, 2449 (1984).
[15] D. P. DiVincenzo and E. J. Mele, Phys. Rev. B **29**, 1685 (1984).
[16] J. P. Carbotte, K. R. Bryenton, and E. J. Nicol, Phys. Rev. B **99**, 115406 (2019).
[17] A. A. Allocca, D. K. Efimkin, and V. M. Galitski, Phys. Rev. B **98**, 045430 (2018).
[18] I. A. Gonoskov, N. Tsatrafyllis, I. K. Kominis, and P. Tzallas, Sci. Rep. **6**, 32821 (2016).
[19] S. Patankar, L. Wu, B. Lu, M. Rai, J. D. Tran, T. Morimoto, D. E. Parker, A. G. Grushin, N. L. Nair, J. G. Analytis, J. E. Moore, J. Orenstein, and D. H. Torchinsky, Phys. Rev. B **98**, 165113 (2018).
[20] G. B. Ventura, D. J. Passos, J. M. B. Lopes dos Santos, J. M. Viana Parente Lopes, and N. M. R. Peres, Phys. Rev. B **96**, 035431 (2017).
[21] T. Huang, X. Zhu, L. Li, X. Liu, P. Lan, and P. Lu, Phys Rev A. **96**, 043425 (2017).
[22] F. De Leonardis, R. A. Soref, and V. M. N. Passaro, Sci. Rep. **7**, 40924 (2017).
[23] S. Ghimire, A. D. DiChiara, E. Sistrunk, P. Agostini, L. F. DiMauro, and D. A. Reis, Nat. Phys. **7**, 138 (2011).
[24] R. I. Woodward, R. T. Murray, C. F. Phelan, R. E. P. de Oliveira, T. H. Runcorn, E. J. R. Kelleher, S. Li, E. C. de Oliveira, G. J. M. Fechine, G. Eda, and C. J. S. de Matos, 2D Mater. **4**, 011006 (2017).
[25] C. Aversa and J. E. Sipe, Phys. Rev. B **52**, 14636 (1995).
[26] H. Ishihara and K. Cho, Phys. Rev. B **48**, 7960 (1993).
[27] R. Eder, A.-M. Janner, and G. A. Sawatzky, Phys. Rev. B **53**, 12786 (1996).
[28] C. Hua Lee, X. Zhang, and B. Guan, Sci. Rep. **5**, 18008 (2015).
[29] T. Jiang, D. Huang, J Cheng, X. Fan, Z. Zhang, Y. Shan, Y. Yi, Y. Dai, L. Shi, K. Liu, C. Zeng, J. Zi, J. E. Sipe, Y. R. Shen, W. T. Liu, and S. Wu, Nat. Photonics **12**, 430 (2018).
[30] X. Dai, L. Jiang, and Y. Xiang, Sci. Rep. **5**, 12271 (2015).
[31] O. Zurrón, A. Picón, and L. Plaja, New J. Phys. **20**, 053033 (2018).
[32] T. Stauber, N. M. R. Peres, and A. K. Geim, Phys. Rev. B **78**, 085432 (2008).
[33] J. L. Cheng and C. Guo, Phys. Rev. B **97**, 125417 (2018).
[34] J. L. Cheng, N. Vermeulen, and J. E. Sipe, New J. Phys. **16**, 053014 (2014).
[35] A. V. Gorbach and E. Ivanov, Phys. Rev. A **94**, 013811 (2016).
[36] H. Rostami and M. Polini, Phys. Rev. B **93**, 161411(R) (2016).
[37] N. Yoshikawa, T. Tamaya, and K. Tanaka, Science **356**, 736 (2017).
[38] E. G. Mishchenko, Phys. Rev. Lett. **103**, 246802 (2009).
[39] W. Wang, C. Zhang, and Z. Ma, J. Phys.: Condens. Matter **24**, 035303 (2012).
[40] Zheng Liu, Matthew Sanderson, J. C. Cao, and C. Zhang, Phys. Rev. B **90**, 235430 (2014).
[41] D. Leykam and A. S. Desyatnikov, Adv. Phys. X **1**, 101 (2016).
[42] A. Raoux, M. Morigi, J.-N. Fuchs, F. Piéchon, and G. Montambaux, Phys. Rev. Lett. **112**, 026402 (2014).
[43] F. Wang and Y. Ran, Phys. Rev. B **84**, 241103(R) (2011).
[44] D. Bercioux, D. F. Urban, H. Grabert, and W. Häusler, Phys. Rev. A **80**, 063603 (2009).
[45] J. Vidal, R. Mosseri, and B. Douçot, Phys. Rev. Lett. **81**, 5888 (1998).
[46] J. Vidal, P. Butaud, B. Douçot, and R. Mosseri, Phys. Rev. B **64**, 155306 (2001).
[47] B. Dóra, J. Kailasvuori, and R. Moessner, Phys. Rev. B **84**, 195422 (2011).
[48] Z. Liu, Z.-F. Wang, J.-W. Mei, Y.-S. Wu, and F. Liu, Phys. Rev. Lett. **110**, 106804 (2013).
[49] M. G. Yamada, T. Soejima, N. Tsuji, D. Hirai, M. Dincá, and H. Aoki, Phys. Rev. B **94**, 081102(R) (2016).
[50] N. Su, W. Jiang, Z. Wang, and F. Liu, Appl. Phys. Lett. **112**, 033301 (2018).
[51] S. Peotta and P. Törmä, Nat. Commun. **6**, 8944 (2015).
[52] E. Tang, J.-W. Mei, and X.-G. Wen, Phys. Rev. Lett. **106**, 236802 (2011).
[53] K. Sun, Z. Gu, H. Katsura, and S. Das Sarma, Phys. Rev. Lett. **106**, 236803 (2011).
[54] T. Neupert, L. Santos, C. Chamon, and C. Mudry, Phys. Rev. Lett. **106**, 236804 (2011).
[55] J. D. Malcolm and E. J. Nicol, Phys. Rev. B **94**, 224305 (2016).
[56] J. D. Malcolm and E. J. Nicol, Phys. Rev. B **92**, 035118 (2015).
[57] W. Häusler, Phys. Rev. B **91**, 041102(R) (2015).
[58] L. Du, X. Zhou, and G. A. Fiete, Phys. Rev. B **95**, 035136 (2017).
[59] Z. Liu, E. J. Bergholtz, H. Fan, and A. M. Läuchli, Phys. Rev. Lett. **109**, 186805 (2012).
[60] T. Louvet, P. Delplace, A. A. Fedorenko, and D. Carpentier, Phys. Rev. B **92**, 155116 (2015).
[61] D. Xiao, M.-C. Chang, and Q. Niu, Rev. Mod. Phys. **82**, 1959 (2010).
[62] Y. Xu and L.-M. Duan, Phys. Rev. B **96**, 155301 (2017).
[63] E. Illes, J. P. Carbotte, and E. J. Nicol, Phys. Rev. B **92**, 245410 (2015).
[64] T. Biswas and T. K. Ghosh, J. Phys.: Condens. Matter **28**, 495302 (2016).
[65] D. F. Urban, D. Bercioux, M. Wimmer, and W. Häusler, Phys. Rev. B **84**, 115136 (2011).
[66] R. Shen, L. B. Shao, Baigeng Wang, and D. Y. Xing, Phys. Rev. B **81**, 041410(R) (2010).
[67] E. Illes and E. J. Nicol, Phys. Rev. B **95**, 235432 (2017).
[68] Y. Betancur-Ocampo, G. Cordourier-Maruri, V. Gupta, and R. de Coss, Phys. Rev. B **96**, 024304 (2017).

[69] T. Biswas and T. Kanti Ghosh, J Phys.: Condens. Matter. **30**, 075301 (2018).
[70] E. Illes and E. J. Nicol, Phys. Rev. B **94**, 125435 (2016).
[71] A. D. Kovács, G. Dávid, B. Dóra, and J. Cserti, Phys. Rev. B **95**, 035414 (2017).
[72] J. D. Malcolm and E. J. Nicol, Phys. Rev. B **93**, 165433 (2016).
[73] S. K. Firoz Islam and P. Dutta, Phys. Rev. B **96**, 045418 (2017).
[74] M. Vigh, L. Oroszlány, S. Vajna, P. San-Jose, G. Dávid, J. Cserti, and B. Dóra, Phys. Rev. B **88**, 161413(R) (2013).
[75] S. K. Firoz Islam and A. Saha, Phys. Rev. B **98**, 235424 (2018).
[76] G. W. Chern, C. C. Chien, and M. Di Ventra, Phys. Rev. A **90**, 013609 (2014).
[77] B. Dóra, I. F. Herbut, and R. Moessner, Phys. Rev. B **90**, 045310 (2014).
[78] C. Z. Wang, H. Y. Xu, L. Huang, and Y. C. Lai, Phys. Rev. B **96**, 115440 (2017).
[79] B. Dey and T. K. Ghosh, Phys. Rev. B **98**, 075422 (2018).
[80] B. Dey and T. K. Ghosh, Phys. Rev. B **99**, 205429 (2019).
[81] D. Huang, A. Lurov, H.-Y. Xu, Y.-C. Lai, and G. Gumbs, Phys. Rev. B **99**, 245412 (2019).
[82] D. O. Oriekhov, E. V. Gorbar, and V. P. Gusynin, Low Temp. Phys. **44**, 1313 (2018).
[83] M.-W. Alam, B. Souayeh, and S. K. Firoz Islam, arXiv:1901.07943.
[84] O. V. Bugaiko and D. O. Oriekhov, J. Phys.: Condens. Matter **31**, 325501 (2019).
[85] Y. R. Chen, Y. Xu, J. Wang, J. F. Liu, and Z. Ma, Phys. Rev. B **99**, 045420 (2019).
[86] E. Ghahramani and J. E. Sipe, Appl. Phys. Lett. **64**, 2421 (1994).
[87] D. J. Moss, E. Ghahramani, J. E. Sipe, and H. M. van Driel, Phys. Rev. B **41**, 1542 (1990).
[88] R. L. Peterson, Rev. Mod. Phys. **39**, 69 (1967).
[89] A. Morita, Phys. Rev. A **34**, 1499 (1986).
[90] A. R. Wright, X. G. Xu, J. C. Cao, and C. Zhang, Appl. Phys. Lett. **95**, 072101 (2009).
[91] Y. S. Ang, S. Shareef, and C. Zhang, Appl. Phys. Lett. **97**, 243110 (2010).
[92] C. Zhang, Phys. Rev. B **66**, 081105(R) (2002).
[93] P. C. E. Stamp and C. Zhang, Phys. Rev. Lett. **66**, 1902 (1991).
[94] S. Blanes, F. Casas, J. A. Oteo, and J. Ros, Phys. Rep. **470**, 151 (2009).
[95] S. Restrepo, J. Cerrillo, V. M. Bastidas, D. G. Angelakis, and T. Brandes, Phys. Rev. Lett. **117**, 250401 (2016).
[96] T. Kuwahara, T. Mori, and K. Saito, Ann. Phys. (NY) **367**, 96 (2016).
[97] V. Novičenko, E. Anisimovas, and G. Juzeliūnas, Phys. Rev. A **95**, 023615 (2017).
[98] A. Eckardt and E. Anisimovas, New J. Phys. **17**, 093039 (2015).
[99] Y. S. Ang and C. Zhang, J. Phys. D: Appl. Phys. **45**, 395303 (2012).
[100] S. Shareef, Y. S. Ang, and C. Zhang, J. Opt. Soc. Am. B **29**, 274 (2012)
[101] F. Giorgianni, E. Chiadroni, A. Rovere, M. Cestelli-Guidi, A. Perucchi, M. Bellaveglia, M. Castellano, D. Di Giovenale, G. Di Pirro, M. Ferrario, and R. Pompili, Nat. Commun. **7**, 11421 (2016).
[102] S. Liu, C. Zhang, M. Hu, X. Chen, P. Zhang, S. Gong, T. Zhao, and R. Zhong, Appl. Phys. Lett. **104**, 201104 (2014).
[103] H. Wang, D. Nezich, J. Kong, and T. Palacios, IEEE Electron Device Lett. **30**(5), 547 (2009).
[104] Q. Wen, W. Tian, Q. Mao, Z. Chen, W. Liu, Q. Yang, M. Sanderson, and H. Zhang, Sci. Rep. **4**, 7409 (2014).